Crustal strain-dependent serpentinisation in the Porcupine Basin, offshore Ireland

Prada, Manel; Watremez, Louise; Chen, Chen; O'Reilly, Brian; Minshull, Timothy; Reston, Timothy; Shannon, Patrick; Klaeschen, Dirk; Wagner, Gerlind; Gaw, Viola

DOI:
10.1016/j.epsl.2017.06.040

Crustal strain-dependent serpentinisation in the Porcupine Basin, offshore Ireland

Manel Prada (1)*, Louise Watremez (2)**, Chen Chen (2), Brian M. O'Reilly (1), Timothy A. Minshull (2), Tim J. Reston (3), Patrick M. Shannon (4), Dirk Klaeschen (5), Gerlind Wagner (5), Viola Gaw (5)

(1) Geophysics Section, Dublin Institute of Advanced Studies, Dublin, Ireland

(2) Ocean and Earth Science, National Oceanography Centre Southampton, University of Southampton, Southampton, UK

(3) School of Geography, Earth and Environmental Sciences, University of Birmingham, Birmingham, UK

(4) School of Earth Sciences, University College Dublin, Dublin, Ireland

(5) Geomar Helmholtz Centre for Ocean Research, Kiel, Germany

*mprada@cp.dias.ie (corresponding author)

** now at UPMC, Univ. Paris 6, Sorbonne Universités, ISTeP, Paris, France

ABSTRACT

Mantle hydration (serpentinisation) at magma-poor rifted margins is thought to play a key role in controlling the kinematics of low-angle faults and thus, hyperextension and crustal breakup. However, because geophysical data principally provide observations of the final structure of a margin, little is known about the evolution of serpentinisation and how this governs tectonics during hyperextension. Here we present new observational evidence on how crustal strain-dependent serpentinisation influences hyperextension from rifting to possible crustal breakup along the axis of the Porcupine Basin, offshore Ireland. We present three new P-wave seismic velocity models that show the seismic structure of the uppermost lithosphere and the geometry of the Moho across and along the basin axis. We use neighbouring seismic reflection lines to our tomographic models to estimate crustal stretching (β_c) of ~2.5 in the north at 52.5° N and > 10 in the south at 51.7° N. These values suggest that no crustal embrittlement occurred in the northernmost region, and that rifting may have progressed to crustal breakup in the southern part of the study area. We observed a decrease in mantle velocities across the basin axis from east to west. These variations occur in a region where β_c is within the range at which crustal embrittlement and serpentinisation are possible (β_c 3-4). Across the basin axis, the lowest seismic velocity in the mantle spatially coincides with the maximum amount

of crustal faulting, indicating fault-controlled mantle hydration. Mantle velocities also suggest that the degree of serpentinisation, together with the amount of crustal faulting, increases southwards along the basin axis. Seismic reflection lines show a major detachment fault surface that grows southwards along the basin axis and is only visible where the inferred degree of serpentinisation is > 15 %. This observation is consistent with laboratory measurements that show that at this degree of serpentinisation, mantle rocks are sufficiently weak to allow low-angle normal faulting. Based on these results, we propose two alternative formation models for the Porcupine Basin. The first involves a northward propagation of the hyperextension processes, while the second model suggests higher extension rates in the centre of the basin than in the north. Both scenarios postulate that the amount of crustal strain determines the extent and degree of serpentinisation, which eventually controls the development of detachments faults with advanced stretching.

1 Introduction

Serpentinisation is a metasomatic reaction of ultramafic rocks that lowers both the seismic velocity and density of the original rock *[e.g., Carlson and Miller, 2003; Christensen, 2004]*, causing volumetric expansion and cracking *[O'Hanley, 1992; Tutolo et al, 2016]*. At rifted margins, this process may occur when crustal-scale faulting takes place, allowing inflow of seawater into the mantle *[e.g. O'Reilly et al., 1996]*. Numerical simulations show that crustal-scale faulting and serpentinisation can occur when the entire crust becomes brittle at a critical stretching factor of 3-4 as long as the rift retains low temperatures (< 600ºC) *[Pérez-Gussinyé and Reston 2001; Guillot et al., 2015]*, which makes serpentinisation a widely recognised process of magma-poor rifted margins.

As inferred from seismic velocity models *[Bayrakci et al., 2016],* serpentinisation at magma-poor rifted margins is not only controlled by the occurrence of crustal-scale faulting but also by total fault displacement. This observation suggests that water can only effectively infiltrate the mantle during the late syn-rift stage when normal faults are still active *[O'Reilly et al., 1996]*. Serpentinisation has important tectonic implications since it reduces the friction coefficient of mantle rocks *[Escartín et al., 2001]*, and causes the formation of secondary minerals that, along with reaction-driven fracturing *[Tutolo et al, 2016]*, causes high fluid pressure *[Moore et al., 1996]*. Weakening of mantle rocks and fluid overpressure are both proposed to have a critical role in the kinematics of low-angle faults like the S detachment along the Galicia Margin *[Reston et al., 2007]*. Additionally, thermo-mechanical simulations based on geophysical and geological observations suggest that the formation of weak regions in the lithosphere causes rift acceleration *[Huismans and Beaumont, 2003; Brune et al.,* 2016*]*, which is critical in shaping rifted margins as it controls their asymmetry *[Huismans and Beaumont, 2003; Brune et al., 2014]*. Hence, understanding the evolution of serpentinisation and its role in controlling tectonic processes at magma-poor rifted margins will provide new insights into the formation of continental passive margins. However, very little is known regarding the evolution of mantle hydration with progressive lithospheric extension. This is because most of the observations are made along mature rifted margins, in which the mantle is already exhumed and seafloor spreading is established *[e.g. Whitmarsh et al., 1996; Funk et al., 2003; Davy et al., 2016]*.

In this work, we focus on the Porcupine Basin, a north-south triangular-shaped basin located in the North Atlantic margin southwest of Ireland (Fig. 1a). The Porcupine Basin is a failed rift in which extension increases dramatically from north to south along the basin axis *[Tate et al., 1993; Watremez et al., 2016]*. This increase makes the Porcupine Basin an ideal natural laboratory to assess the variations of formation processes related to progressive lithospheric stretching. We present a set of P-wave seismic velocity (V_P) models derived from travel time tomography of wide-angle seismic (WAS) data acquired in the Porcupine Basin (Fig. 1a). The models reveal the seismic structure of the

crust and uppermost mantle, as well as the geometry of the Moho across and along the basin axis from the northern (~52.5º N) and less extended region of the basin, to the central region (~51.5º N), where hyperextension occurred due to advanced tectonic stretching *[e.g. Reston et al., 2001, 2004]*. Careful analysis of uppermost mantle V_p from our models suggest along- and across-axis variations in mantle hydration. We use gravity data and seismic reflection profiles near our V_p models to explore potential reasons for such variations, and assess their implications for the formation of the Porcupine Basin.

2 Tectonic setting

The Porcupine Basin was formed in response to several rift and subsidence phases during the Late Paleozoic and Cenozoic, with the most pronounced rift phase occurring in Late Jurassic–Early Cretaceous times *[Tate et al., 1993; Naylor and Shannon, 2011]*. Subsidence curves *[Tate et al., 1993]* suggest that axial stretching factors (i.e., $\beta_c=T_0/T_1$; *T_0 is initial crustal thickness before extension, and T_1 the current crustal thickness)* increase from 1.5-2 in the north to 3-4 in the central region. However, WAS data *[Watremez et al., 2016]* and seismic reflection data *[Reston et al., 2004]* both show that maximum β_c are at least 3 and 2 times greater than these estimates in the northern and central parts of the basin, respectively. This discrepancy can be explained by mantle serpentinisation, which reduces the density of mantle rocks, and therefore reduces the effect of thermal subsidence. A similar effect is inferred from seismic data in the Rockall Basin, northwest of the Porcupine Basin in the North Atlantic *[O'Reilly et al., 1996]*.

Mantle hydration in the Porcupine has been proposed by many authors based on geophysical data *[Reston et al., 2001, Readman et al., 2005; O'Reilly et al., 2006; Watremez et al., 2016]*. Gravity data reveal a major positive free air gravity anomaly between 51.5º-52.5ºN (Fig. 1b) that suggests the presence of extremely thin crust and a low density uppermost mantle (i.e., < 3.3 g/cm^3). This anomaly is also associated with a major tectonic feature known as the Porcupine Arch *[Naylor et al., 2002]*, recognised on seismic reflection profiles as a deep, bright and continuous package of high-amplitude reflectivity *[Johnson et al., 2001; Reston et al., 2001; Naylor et al., 2002]*. The Porcupine Arch was previously interpreted either as the top of the crystalline crust *[Johnson et al., 2001; Naylor et al., 2002]*, or as a detachment surface (i.e., the P-detachment) representing the Moho (i.e. crust-mantle boundary) *[Reston et al., 2001, 2004]*. WAS data modelling has revealed V_p between 7.5 and 8 km/s below the Porcupine Arch *[O'Reilly et al., 2006; Watremez et al., 2016]*, which is too high for continental crust but not for serpentinised mantle rocks *[Carlson and Miller, 2003]*. This result not only supports the hypothesis that the Porcupine Arch is the Moho, but also suggests that the mantle below is partially serpentinised [i.e. ~ 10-20%; *O'Reilly et al., 2006*]. Interestingly, *Reston et al.*

111 *[2001, 2004]* noted the presence of major faults crosscutting the entire syn- and pre-rift section up to
112 the top of the Arch, implying that crustal embrittlement has occurred in the Porcupine Basin, further
113 supporting the hypothesis of a serpentinised mantle.

114 3 Wide-angle seismic data analysis and modelling

115 In 2004, three WAS profiles were collected along pre-existing reflection profiles across the Porcupine
116 Basin *[Reston et al., 2001, 2004]* (Fig. 1a). Up to 24 four-component ocean-bottom seismometers
117 (OBS) and ocean-bottom hydrophones (OBH) were used to acquire the data along each of the three
118 lines presented here (Fig. 1a). The receivers were spaced every ~8 km along each line and the seismic
119 source was generated by 2-3 32 litre (2000 in^3) airguns fired every 60 s (~120 m).

120 Seismic refraction data processing involved a predictive deconvolution and a bandpass filter defined
121 by frequencies of 1-5-15-25 Hz. The data show clear refraction and reflection travel times
122 corresponding to the sedimentary section, the crystalline basement and the uppermost mantle (Fig.
123 2). In particular, the data show a prominent phase at large offsets with apparent velocity of 8 km/s
124 that has been interpreted as a refracted phase through the uppermost mantle or P_n (e.g., >40 km model
125 offset in Figs. 2 and 3d). A high-amplitude reflection identified at shorter offset than P_n arrivals has
126 been interpreted as the critical reflection at the Moho or P_mP (Figs. 2 and 3). Overall, we manually
127 picked a total of 28,995 travel times of refracted and reflected phases for line P02, 31,676 for line
128 P03, and 35,708 for line P04. Picking uncertainties were automatically assigned between 20 and 125
129 ms based on the signal to noise ratio of the trace 250 ms before and after the picked arrival time,
130 following the empirical relationship of Zelt & Forsyth (1994).

131 The data were inverted for V_p structure and geometry of seismic interfaces (e.g., Moho) using the
132 method of *Korenaga et al. [2000]*. This method computes the travel time residuals by calculating the
133 shortest ray-path for each travel time, and solves a linearised inversion problem to minimise the travel
134 time residuals. The V_p models were obtained following a layer stripping strategy *[e.g. Sallarès et al.,*
135 *2011]*, so that refracted and reflected travel times of each layer were inverted sequentially from near
136 to far offset, resolving at each step the velocity and depth of each layer of the model from the shallow
137 sediments to the uppermost mantle. Travel times of critical reflections at sedimentary interfaces were
138 identified in all the lines (Figs. 2 and A1), and included in the layer stripping (see Fig. A2 for layer
139 stripping sequence of each model). However, given that the main goal of the study relies on the deep
140 structure of the basin, we only show the geometry of the Moho interface (blue thick lines in Fig. 4).
141 The grid spacing for P04 was optimally set at 0.25 x 0.25 km, whereas for P03 and P02 it varies
142 vertically from 0.1 km at the top to 0.5 km at the bottom, and it was held constant horizontally along
143 the grid at 0.3 km. The finer grid spacing at shallow levels along dip lines P03 and P02 was designed

to allow for seismic heterogeneity caused by sedimentary structures associated to the margins of the basin. The grid spacings chosen are much smaller than the anomaly size (i.e. >10 km wide) that we can retrieve at the depths of interest (i.e. ~15 depth). Thus, these grids are optimum for the purpose of the study.

Regularisation parameters are defined by a set of horizontal and vertical correlation lengths that vary from top to bottom in the grid. Horizontal correlation lengths (HCL) were 3 km at the top of all models and increased to 10-12 km at the bottom of the grid. Vertical correlation length (VCL) was 0.2-0.5 km at the top of the grid and 5-8 km at the bottom of the grid. Reflector correlation lengths (RCL) were set at 4 km and the depth kernel-scaling factor *(W)* was 0.1-0.5. Overall, tomographic models in Fig. 4 have a good data fit as root mean square of residual travel times are around half of the dominant wavelength (i.e. 20-30 ms for sediment phases, and ~50ms and ~80ms for crustal and mantle phases, respectively; see Tables A1 to A3 for further details of root mean square values).

3.1 Model parameter uncertainty

The range of uncertainty values of V_p and depth of the Moho was assessed by means of a Monte-Carlo analysis. The approach was performed for each of the different layers following the same layer-stripping strategy applied for the inversion of the preferred models in Fig. 4. In this case, for each layer, we produced 100 realisations (120 for line P04). Each realisation consisted in a travel-time dataset with added random noise (up to ±125 ms), an input model for the corresponding layer with a random 1D velocity-depth distribution (±10% and ±6% for crustal and mantle velocities, respectively), and a flat reflector with a random depth (±4 km for the Moho). HCL, VCL, RCL and *W* were also randomised during the Monte-Carlo analysis (HCL 5±2 km and 15±5 km and VCL 0.5±0.2 km and 6±2 km at the top and bottom of the model, respectively; RCL 5±1 km; *W* between ~0.1 and ~1). This process allowed us to assess the optimum range of regularisation parameters, which resembles the range used to obtain the preferred models of Fig. 4. The standard deviation of the inverted 100 models (120 for line P04) was computed and taken as a statistical measure of the uncertainty of the model parameters *[Tarantola, 1987; Korenaga et al., 2000]* (Fig. 5).

Overall, the V_p structure of the three models is well constrained in areas with a good ray coverage (see Fig. A3 for ray coverage information). The standard deviation (i.e., statistical uncertainty) of velocities in lines P02 and P03 ranges between 0.1 and 0.3 km/s (Fig. 5), whereas it is < 0.2 km/s for line P04 (Fig. 5). In particular, uppermost mantle velocities are generally well constrained with values < ±0.2 km/s, except along line P02 where locally they reach ~±0.3 km/s (Fig. 5). Higher uncertainties along P02 are the result of combining a high pick uncertainty (i.e. ~125 ms) of P_n phases with a lower ray coverage in that particular area of the model (i.e. between 120 and 140 along P02 Figs. 5 and A3). The Moho depth is well constrained in the centre of the models with uncertainties < ±0.2 km (Fig. 5),

whereas it is less constrained towards the edges of the model given the lack of P_mP arrivals (see Fig. A4 for ray tracing of P_mP arrivals).

4 Results

The northernmost W-E profile P03 runs across the northern Porcupine Basin and shows a sedimentary basin fill displaying V_p between 1.5 and 4.0-4.5 km/s that thickens towards the centre of the basin, reaching 8-9 km thick *[Watremez et al., 2016]*. Syn-rift sediments are represented by V_p between 4.5 and 5.0 km/s and basement velocities range from 5.0-5.5 to 6.6-6.8 km/s, that is typical for crystalline continental crust *[Christensen & Mooney, 1995]* (Fig. 4). The Moho obtained from inversion of P_mP arrivals shallows to 15 km depth at ~ 130 km of profile distance (Fig. 4a). Below this thinnest section of the crust (km 115-145), the uppermost mantle V_p is not only slower than unaltered peridotite (i.e., 8.0 km/s), in agreement with previous studies *[O'Reilly et al., 2006]*, but also decreases by 0.4 km/s from east to west, from ~8.0 to ~7.6 km/s (Fig. 6a).

The southernmost dip line P02 is located in the southern region of the study area (Fig. 1), and shows a similar sedimentary cover with V_p between 1.5 and 4.0-4.5km/s that can be up to ~8 km thick. Basement velocities in the margins are similar to P03, ranging from 5.0-5.5 to 6.6-6.8 km/s, but they barely exceed 6.0 km/s in the basin centre, where the crust is thinnest (e.g. between 120 and 150 km of profile distance in Fig. 4c). From the neighbouring reflection line 106 (Fig. 7), we observe that crustal $V_p < 6.0$ km/s spatially coincides with a pervasively faulted sequence (e.g. between 120-150 km of profile distance in Fig. 7a), which appears to comprise both basement and highly rotated syn-rift sediments *[Reston et al., 2004]*. The P_mP-derived Moho along P02 shallows up to ~11 km depth (Fig. 4c), that is 2 km shallower than the Moho along P03, indicating that extension increases southwards along the basin axis. Mantle velocities are slower than those of pristine mantle rock and are characterised by strong lateral variations, similar to P03. In this case, however, V_p decreases up to 1 km/s from east to west, from 8.0-8.2 to 7.0-7.2 km/s (Fig 6b).

The N-S line P04 runs along the basin axis crossing profiles P03 and P02 (Fig 1 and 4). The sedimentary cover with V_p between 1.5 and 4.0-4.5 km/s, previously imaged by P03 and P02 across the basin axis, is also imaged along the basin axis thinning subtly from north to south ~1-2 km (Fig. 4a). Beneath this, crustal V_p increases with depth from 5.0-5.5 to 6.4-6.6 km/s (Fig. 4a). The resolved Moho shallows from 20 km deep in the north to ~11 km in the south, which denotes again a significant crustal thinning from north to south along the basin axis (Fig. 4a). In agreement with the rest of the profiles, velocities in the uppermost mantle are slower than 8.0 km/s. However, no significant variations of mantle velocities are observed along the profile except at km 110, where mantle V_p increases gently in the uppermost section of the mantle, from north to south (Fig. 4a).

5 Discussion

5.1 Variations of mantle hydration across the basin axis

The tomographic results along dip lines show across-axis variations in uppermost mantle V_p (Figs. 6a and 6b). In both cases, seismic velocities increase towards the east where seismic velocity can be up to 1 km/s faster (i.e., case for P02, Fig. 6b). Comparing the vertical seismic structure of W-E lines P03 and P02 with N-S line P04 at the corresponding intersection points (Figs. 6c and 6d), we observe small differences that are within the velocity error (i.e. up to 0.2 km/s in Figs. 6c and 6d). Hence, we cannot conclude whether these small variations are due to variations in model parametrisation, to data uncertainties, or to anisotropy. If anisotropy was the main contributor to such variations, its effect is still too small to explain across-axis velocity variations in the uppermost mantle (i.e. Figs.6a and 6b).

Anisotropy is suggested to be caused by alignment of cracks, damage zones and serpentinisation within fault zones in the outer rise of subduction zones (with the slowest propagation perpendicular to fault zone) *[Miller and Lizarralde, 2016]*. However, the faulting responsible for mantle hydration in this setting [i.e. bending-related faulting; *Ranero et al., 2003]* is closer to the vertical than that responsible for extension in the Porcupine *[Reston et al., 2004]*. Hence, the small discrepancy of seismic wave speed between W-E and N-S propagation in the Porcupine Basin may be explained by the low-angle orientation of damage zones in the W-E direction (the approximate direction of extension). This orientation would result in a similar propagation of refracted seismic waves (i.e. subhorizontal propagation) in both W-E and N-S directions, and reduce azimuthal anisotropy caused by alignment of damage zones. Hence, variations of mantle V_p across the basin axis potentially reflect petrological variations, which in this case may indicate differences in the degree of magmatic intrusion and/or serpentinisation.

Geological observations from boreholes *[Tate & Dobson, 1988],* coupled with seismic stratigraphic interpretation *[Reston et al., 2004],* suggest that there was little syn-rift magmatism in the northern and southern region of the study area (i.e. 51.5º to ~53º N; Fig. 1). Sills intruded in the post-rift sequence at ~60-61 Ma (i.e., early Paleocene) indicate the first major magmatic activity *[Tate & Dobson, 1988]*. As observed in other regions in the North Atlantic *[e.g., Archer et al., 2005]* the intrusion of magmatic bodies after the deposition of post-rift sediments drives significant uplift and consequent deformation of the older post-rift sequence (mostly Cretaceous in our case). However, seismic reflection lines reveal no domal deformation in the Cretaceous unit (Fig. 7a) that could be attributed to such effects. Instead, a flat and undeformed post-rift sequence is observed, suggesting that early Cenozoic magmatism (crustal intrusion and underplating) is an unlikely explanation for low subcrustal velocity variations.

Alternatively, mantle serpentinisation has been proposed during the formation of the basin *[Reston et al., 2001, 2004; Readman et al., 2005; O'Reilly et al., 2006]*. Numerical modelling of evolving rheology and temperature *[Pérez-Gussinyé and Reston 2001]* predicts that at stretching factors of 3-4 the crust becomes entirely brittle and the subcrustal mantle cools enough (<600ºC) to serpentinise at rifting rates appropriate for the Porcupine Basin *[Reston et al., 2004]*, especially in the absence of voluminous syn-rift magmatism *[Tate & Dobson, 1988]* to advect heat.

The degree of extension in the northern region of the basin has been assessed in *Watremez et al. [2016]* by combining velocity model P03 with its coincident seismic line Wire2 (Fig. 1). The result of this combination reveals that the minimum crustal thickness along P03 is ~5 km, corresponding to a β_c of ~6 (at ~120 km of profile distance; Fig. 4b), assuming an original crustal thickness of ~30 km SW of Ireland *[Lowe & Jacob, 1989; O'Reilly et al., 2010]*. This amount of extension is well within the range at which crustal embrittlement is expected *[i.e. 3-4 in Pérez-Gussinyé and Reston 2001]*.

In the south, the comparison between the seismic reflection line 106 and the velocity model along P02 shows that the geometry of the P-detachment resembles that of the WAS-derived Moho (Fig 7b). Particularly, between km 140 and 155 the WAS-derived Moho follows the base of reflections associated with the Moho according to *Reston et al [2001]*. However, some discrepancies exist between these two seismic interfaces. Towards the east, between km 155 and 165 (Fig. 7b), the WAS-derived Moho is slightly shallower (i.e. < 0.5 s two-way time) than the eastward-dipping reflections interpreted by *Reston et al [2001]* as the Moho (Fig. 7). Given that the fault plane of the detachment and the eastward-dipping reflections associated with the Moho are close to each other in this particular area, such discrepancy could be attributed partly by cycle-skipping in P_mP arrival times. Further discrepancy is observed towards the west, between km 135 and 140 (Fig. 7b), where the P-detachment in the reflection is steeper than the tomographically resolved Moho (Fig. 7b). In this case, a single strong impedance contrast is observed in the reflection line, which makes cycle-skipping unlikely. Alternatively, seismic reflection lines (Fig. 7) reveal that the P-detachment flattens rapidly along the basin axis from north to south. Hence, given that line P02 was acquired 5 km south of 106 it is likely that the geometry of the P-detachment varies from line 106 to P02 farther south. Also, the smoothing inherent in the inversion might have contributed to this difference. Regardless of these discrepancies, the wide-angle reflection modelled as the Moho is defined by a significant velocity contrast (> 1.5 s^{-1}) and it overlies material with V_p ~8 km/s, making this interface an ideal candidate for the Moho. Our results thus support the hypothesis of *Reston et al. [2001]* that most of the P-detachment forms a tectonic boundary between the crust and the mantle, and that crustal faulting associated with the P-detachment would have facilitated mantle serpentinisation.

277 The combination of the reflection line 106 and model P02 also allows us to provide some estimates
278 of crustal thickness. We infer that the crystalline basement, if any, in the most extended region along
279 line P02 could be as thin as 2 km (i.e., between 140 and 155 km of line P02, Fig. 7), which implies a
280 $\beta_c > 10$. At this degree of extension, rifting could have reached breakup, which means that syn-rift
281 sediments (now exhibiting crustal velocities) could be deposited directly on the mantle in this region
282 of the central Porcupine Basin. This configuration would imply that a substantial part of the rift
283 process has been accompanied by ongoing serpentinisation, which is in agreement with low mantle
284 V_p observed along model P02 (i.e. ~ 7.0-7.5 km/s in Fig. 6b).

285 To test V_p from our models and explore the hypothesis of variations in mantle hydration across the
286 Porcupine Basin axis we performed gravity modelling following the method of *Korenaga et al.*
287 *[2001]*. We tested two possible scenarios: a model with homogeneous unaltered mantle, and a model
288 with lateral variations of density in accordance with seismic velocities. This way, V_p from our models
289 was converted to density (ρ) using the V_p-ρ relationships of *Hughes et al. [1998]* for sediments and
290 *Christensen & Mooney [1995]* for the crystalline continental crust. For the mantle, a ρ of 3.3 g/cm^3
291 was assumed for the first scenario, while *Carlson and Miller's [2003]* relationship for serpentinised
292 mantle rocks was used to test the second scenario. The results show that for both lines P02 and P03
293 the best-fitting gravity anomaly is that derived from ρ models of the second scenario, in which
294 densities in the uppermost mantle vary across the basin axis (Fig. 8). These results support V_p
295 obtained from travel time tomography and a heterogeneous hydration of the mantle.

296 We compare the tectonic structure with the velocity field (Fig. 7b) to explore for potential reasons for
297 such variations in mantle hydration. This comparison reveals that crustal faulting in the Porcupine
298 Basin is spatially denser above the lowest mantle V_p (i.e., highest degree of serpentinisation), whereas
299 it is less intense above areas where mantle V_p is higher (i.e., lower degree of serpentinisation) (Fig.
300 7b). This correlation suggests that crustal-scale faulting has controlled mantle hydration in the
301 Porcupine Basin, similar to the Galicia margin, where it has been suggested that water supply to the
302 mantle occurred when faults were active *[Bayrakci et al., 2016]*.

303 ### 5.2 Along-axis variations of mantle hydration: implications for the formation of the
304 Porcupine Basin

305 The comparison between dip lines P03 and P02 shows that mantle V_p decreases from north to south
306 in those areas where the inferred degree of mantle hydration is higher along both models (Fig. 9b).
307 This observation suggests a southward increase in the degree of serpentinisation along the basin axis,
308 from 15-20 % to 25-35% (Fig. 9b). Interestingly, seismic reflection lines show that the P-detachment
309 is only visible south of line Wire2 (Fig. 9c) *[Klemper and Hobbs 1991]*, where the inferred degree of
310 hydration is higher than 15% (Fig. 9b). This correlation is consistent with laboratory measurements,

311 which indicate that a 10-15% degree of serpentinisation is needed to reduce significantly the friction
312 coefficient of the original mantle rock, allowing the development of low-angle normal faults
313 *[Escartín et al., 2001; Reston et al., 2007]*.

314 Given the relevance of crustal faulting in controlling mantle hydration, we looked for along-axis
315 variations in crustal faulting. Seismic reflection line Wire2 (Figs. 1 and 9), coincident with line P03,
316 displays the lowest quality at depth of the four seismic reflection lines shown in Fig. 9c as it was
317 acquired with the shortest streamer *[i.e. 4 km; Klemper and Hobbs 1991]*. Hence, crustal faults are
318 poorly imaged in depth compared to line PAD (10 km long streamer), 103 and 106 (6 km long
319 streamer), all acquired with a longer streamer than Wire2 (4 km long streamer). Despite this quality
320 issue, Wire2 clearly images one crustal fault (Fig. 9c) reaching the WAS-derived Moho (blue dashed
321 line in Fig. 9c). Southwards from Wire2, seismic lines PAD, 103 and 106 show the surface of the P
322 detachment (white dots in Fig. 9c), which becomes larger southwards together with the number of
323 seismically resolved crustal faults (red dashed lines in Fig 9c). In particular, the syn-rift section along
324 the southernmost seismic line 106 contains at least seven faults that crosscut the entire section down
325 to the P-detachment. Velocities along P02 are < 6km/s in the lower crust (i.e. between km 130 and
326 145 of Fig. 7), which is in agreement with the highest concentration of faulting. Overall, the seismic
327 reflection lines in Fig. 9c show that crustal faulting in the Porcupine Basin increases southwards in
328 agreement with the degree of extension, and mantle hydration.

329 We have compared the V_p-derived degree of serpentinisation from those areas of models P02 and
330 P03 where mantle V_p is lowest and ray coverage is satisfactory (Fig. 10), with the amount of
331 seismically-resolved crustal faulting along their corresponding neighbouring seismic reflection lines
332 (i.e., Wire2 for P03, and 106 for P02). This comparison illustrates the good correlation between the
333 degree of mantle hydration and the number of crust-penetrating normal faults along the basin axis
334 (Fig. 10). However, there is no apparent impedance contrast between the syn- and pre-rift section
335 within half-grabens (Fig. 9c), and no well has been drilled that deep (i.e. > 8 km), so we cannot
336 reliably estimate fault displacements. Thus, we cannot assess whether the number of faults or the fault
337 displacement *[Bayrakci et al., 2016]* is more important in controlling access of water to the uppermost
338 mantle in the Porcupine Basin.

339 Regardless of the displacement of faults, our results provide observational evidence of the
340 development of tectonic features related to progressive stretching and serpentinisation along the axis
341 of the Porcupine Basin. As shown by dip lines P03 and P02, the degree of extension increases
342 southwards. This is better illustrated by model P04 (Fig. 4a), in which a β_c of ~2.5 can be estimated
343 in the northernmost section of the basin - assuming a V_p of ~5.5 km/s as the top of the crystalline
344 basement - increasing to $\beta_c > 10$ in the southern part of the study area (~ 51.7ºN). The low degree of

extension in the northernmost section of the basin suggests that crustal embrittlement may not have occurred in this region *[$\beta_c < 3$; Pérez-Gussinyé and Reston 2001]*. Thus, based on line P04, the along-axis transition between rifting and potential crustal breakup occurs over a distance of 80 km. Within this transition, the degree of serpentinisation increases towards the south, where it reaches maximum values of ~35-40% (Fig. 10). In addition, as the degree of serpentinisation increases the P-detachment becomes more important as its surface grows southwards (Fig. 7b).

Based on these observations, one possible formation model of the basin is that crustal embrittlement and mantle serpentinisation started in the south of our study area. Increased serpentinisation (> 15%) and extension then caused the formation of the P-detachment in the same region, creating a weak spot in the rift. Then, progressive lithospheric stretching allowed the propagation of crustal deformation to the north along the basin axis. As long as crustal faults remained permeable enough to percolate water to the mantle and rift temperatures were <~600ºC, serpentinisation and the development of the P-detachment would have also propagated along the basin axis in agreement with the degree of stretching. This scenario implies that hyperextension occurred first in the southern region of our study area and propagated to the north of the basin later.

Alternatively, crustal embrittlement, serpentinisation and development of low-angle faults might have occurred contemporaneously along the basin axis. Since the amount of extension increases southwards, more crustal faults would have developed in the centre of the basin than in the north. Thus, more water would have accessed the mantle in the central region than in the north favouring faster serpentinisation and development of detachment faults. This scenario implies that the central region has opened at higher rates than the northern basin. Given the importance of extension rates in controlling partial decompression melting during lithospheric stretching *[Reid and Jackson 1981; Pérez-Gussinyé et al., 2006]*, this latter scenario could explain the presence of voluminous magmatism in the south Porcupine Basin *[Calves et al., 2012; Watremez et al., 2016]*. Thus, we consider this second scenario as our preferred model of the basin formation, as it is compatible with tectonic and inferred magmatic events further south in the Porcupine Basin. However, our data do not allow us to distinguish between both models, as they fail to provide chronological information of the syn-rift sequence related to crustal faulting along the basin axis. Further data (i.e. well and 3D seismic data) are needed in the centre and southern region of the Porcupine Basin to more fully understand the formation of the basin.

Overall, despite of their different assumptions regarding the timing of tectonic events, in both models the initial distribution of crustal deformation during rifting controls the location and extent of serpentinisation, which together with the amount of extension, governs the onset and growth of detachment faults, and hence of hyperextension in the Porcupine Basin.

6 Conclusions

The V_p models presented in this study show the uppermost lithospheric seismic structure and the geometry of the Moho, across and along the Porcupine Basin axis with unprecedented detail. The velocity structure shows an 8-9 km thick post-rift sedimentary blanket with V_p between 1.5 and 4.5 km/s. The underlying basement displays V_p between 5.0-5.5 to 6.6-6.8 km/s, except for some areas along P02 where lower crustal velocities are < 6.0 km/s. The combination of seismic reflection line 106 and model P02 reveals that V_p < 6.0 km/s are associated to a high degree of fracturing.

The combination of V_p models with the tectonic structure allows us to estimate β_c along each tomographic model. Our results confirm that the degree of extension increases dramatically southward from $\beta_c \sim 2.5$ in the north of the basin to > 10 in the southern part of the study area (~ 51.5º N). Low β_c values in the north imply that no crustal embrittlement occurred in this region of the Porcupine Basin. Based on these results, the along-axis transition between rifting and potential crustal breakup occurs over an 80 km region in the Porcupine Basin axis.

Velocity models also reveal that mantle velocities decrease from east to west up to 1 km/s across the basin axis. These velocities can be explained either by variations in the presence of subcrustal magmatic rocks or mantle serpentinisation. The lack of voluminous syn-rift magmatism in this area of the Porcupine Basin is difficult to reconcile with the first hypothesis, and the presence of major crustal faults spatially coinciding with the lowest subcrustal V_p suggests that faults controlled mantle hydration in the Porcupine Basin.

The comparison between P03 in the north and P02 in the south reveals that the degree of serpentinisation increases southwards from 15-20 % to 25-35%. This is consistent with the fact that the P-detachment is only visible south of P03, where the degree of alteration is > 15 %, and hence sufficient for low-angle faulting *[Escartín et al., 2001; Reston et al., 2007]*. Our results show that along-axis variations in the degree of serpentinisation correlate linearly with the number of crustal faults identified along seismic reflection lines.

Based on the seismic and tectonic structure of the basin presented here we suggest two likely scenarios of basin formation. The first one postulates that crustal embrittlement, serpentinisation and hyperextension occurred first in the southern region of the study area and then propagated northward. The second scenario proposes that serpentinisation and crustal deformation occurred contemporaneously along the basin axis implying faster rates of extension in the south than in the north. In both scenarios, the original distribution of crustal faulting determines the location and extent of serpentinisation, which eventually governs the kinematics of detachment faults.

411 Overall, our work presents for the first time observational evidence of crustal strain-dependent
412 serpentinisation in the Porcupine Basin and its implications for the development of tectonic processes
413 related to hyperextension.

414

415 *ACKNOWLEDGMENTS*

416 This project is funded by the Irish Shelf Petroleum Studies Group (ISPSG) of the Irish Petroleum
417 Infrastructure Programme Group 4. Gravity and seismic line PAD was provided by the Petroleum
418 Affairs Division of the Department of Communications, Climate Action and Environment, Ireland.
419 Seismic reflection data SPB97-103/106 were supplied by Fugro-Geoteam through Conoco-Phillips.
420 Wide-angle seismic data collection was funded by the Deutsche Forschungsgemeinschaft through
421 grant Re 873/10 and was enabled by the professionalism and skill of the officers and crew of the FS
422 Meteor during cruise M61-2. Profile Wire2 was acquired during the BIRPS WIRE project, which was
423 funded by the Natural Environment Research Council (UK), the Department of Energy (Ireland) and
424 Western Geophysical. T.A. Minshull was supported by a Wolfson Research Merit award. We would
425 like to acknowledge the Editor John P. Brodholt and two anonymous reviewers for a very thorough
426 review that helped to improve the manuscript. Generic Mapping Tools [Wessel and Smith, 1998] and
427 Seismic Unix software package [Stockwell, 1999] were used in the preparation this manuscript.

428 **References**

429 Archer, S. G., Bergman, S. C., Iliffe, J., Murphy, C. M., & Thornton, M. (2005). Palaeogene igneous rocks
430 reveal new insights into the geodynamic evolution and petroleum potential of the Rockall Trough, NE
431 Atlantic Margin.Basin Research, 17(1), 171-201. DOI: 10.1111/j.1365-2117.2005.00260.x

432 Bayrakci, G., Minshull, T. A., Sawyer, D. S., Reston, T. J., Klaeschen, D., Papenberg, C., et al. (2016). Fault-
433 controlled hydration of the upper mantle during continental rifting. Nature Geoscience, (March), 1–6.
434 http://doi.org/10.1038/ngeo2671

435 Brune, S., Heine, C., Pérez-Gussinyé, M., & Sobolev, S. V. (2014). Rift migration explains continental margin
436 asymmetry and crustal hyper-extension. Nature Communications, 5. DOI: 10.1038/ncomms5014

437 Brune, S., Williams, S. E., Butterworth, N. P., & Müller, R. D. (2016). Abrupt plate accelerations shape rifted
438 continental margins. Nature, 1–4. http://doi.org/10.1038/nature18319

439 Calvès, G., Torvela, T., Huuse, M., and Dinkleman, M. G. (2012). New evidence for the origin of the Porcupine
440 Median Volcanic Ridge: Early Cretaceous volcanism in the Porcupine Basin, Atlantic margin of
441 Ireland. Geochemistry, Geophysics, Geosystems, 13(6).
442 Carlson, R. L., & Miller, D. J. (2003). Mantle wedge water contents estimated from seismic velocities in
443 partially serpentinised peridotites. Geophysical Research Letters, 30, 12–15.
444 http://doi.org/10.1029/2002GL016600
445 Christensen, N. I. (2004). Serpentinites, peridotites, and seismology. International Geology Review, 46(9),
446 795-816.
447 Christensen, N. I., & Mooney, W. D. (1995). Seismic velocity structure and composition of the continental
448 crust: A global view. Journal of Geophysical Research, 100, 9761. http://doi.org/10.1029/95JB00259
449 Davy, R. G., Minshull, T. A., Bayrakci, G., Bull, J. M., Klaeschen, D., Papenberg, C., et al. (2016). Continental
450 hyperextension, mantle exhumation, and thin oceanic crust at the continent-ocean transition, West
451 Iberia: New insights from wide-angle seismic. Journal of Geophysical Research: Solid Earth, 121,
452 3177–3199.
453 Funck, T., Hopper, J. R., Larsen, H. C., Louden, K. E., Tucholke, B. E., & Holbrook, W. S. (2003). Crustal
454 structure of the ocean-continent transition at Flemish Cap: Seismic refraction results. Journal of
455 Geophysical Research: Solid Earth, 108(B11).
456 Escartín, J., Hirth, G., & Evans, B. (2001). Strength of slightly serpentinised peridotites: Implications for the
457 tectonics of oceanic lithosphere. Geology, 29(11), 1023-1026.
458 Guillot, S., Schwartz, S., Reynard, B., Agard, P., & Prigent, C. (2015). Tectonic significance of serpentinites.
459 Tectonophysics, 646, 1-19. http://dx.doi.org/10.1016/j.tecto.2015.01.020
460 Hughes, S., Barton, P., & Harrison, D. (1998). Exploration in the Shetland-Faeroe Basin using densely spaced
461 arrays of ocean-bottom seismometers. Geophysics, 2, 490–501.
462 Huismans, R. S., and Beaumont, C. (2003). Symmetric and asymmetric lithospheric extension: Relative effects
463 of frictional-plastic and viscous strain softening, J. Geophys. Res., 108(B10), 2496,
464 doi:10.1029/2002JB002026.
465 Johnson, H., J. Ritchie, R. Gatliff, J. Williamson, J. Cavill, and J. Bulat (2001), Aspects of the structure of the
466 Porcupine and Porcupine Seabight basins as revealed from gravity modelling of regional seismic

transects, Geological Society, London, Special Publications, 188(1), 265-274. doi:10.1144/GSL.SP.2001.188.01.15

Klemper, S., and Hobbs, R., (1991). The BRIPS Atlas. Deep seismic reflection profiles around the British Isles. Cambridge University Press, Cambridge, pp. 124

Korenaga, J., Holbrook, W. S., Kent, G. M., Kelemen, P. B., Detrick, R. S., Larsen, H. C., Hopper, J. R. & Dahl-Jensen, T. (2000). Crustal structure of the southeast Greenland margin from joint refraction and reflection seismic tomography. Journal of Geophysical Research - Solid Earth, 105, 21591-21614, doi:10.1029/2000JB900188.

Korenaga, J., Holbrook, W. S., Detrick, R. S., & Kelemen, P. B. (2001). Gravity anomalies and crustal structure at the southeast Greenland margin. Journal of Geophysical Research: Solid Earth, 106, 8853-8870.

Lowe, C., and Jacob, A.W.B., (1989). A north-south seismic profile across the Caledonian suture zone in Ireland. Tectonophysics 168, 297–318.

Miller, N. C., and D. Lizarralde (2016), Finite-frequency wave propagation through outer rise fault zones and seismic measurements of upper mantle hydration, Geophys. Res. Lett., 43, 7982–7990, doi:10.1002/2016GL070083.

Moore, D. E., Lockner, D. A., Summers, R., Shengli, M. A., & Byerlee, J. D. (1996). Strength of chrysotile-serpentinite gouge under hydrothermal conditions: Can it explain a weak San Andreas fault?.Geology, 24(11), 1041-1044.

Naylor, D., P. Shannon, & N. Murphy (2002), Porcupine-Goban Region: A Standard Structural Nomenclature System, Department of the Marine and Natural Resources, Petroleum Affairs Division.

Naylor, D. & Shannon, P.M. (2011). Petroleum Geology of Ireland. Dunedin Academic Press, Edinburgh, Scotland. pp.262.

O'Hanley, D. S. (1992). Solution to the volume problem in serpentinisation. Geology, 20, 705–708.

O'Reilly, B.M., Hauser, F., Jacob, A.W.B. & Shannon, P.M. (1996). The lithosphere below the Rockall Trough: wide-angle seismic evidence for extensive serpentinisation. Tectonophysics, 255, 1-23, doi:10.1016/0040-1951(95)00149-2.

O'Reilly, B.M., Hauser, F., Readman, P.W. (2010). The fine-scale structure of upper continental lithosphere from seismic waveform methods: insights into Phanerozoic crustal formation processes. Geophysical Journal International 180 (1), 101–124.

O'Reilly, B. M., Hauser, F., Ravaut, C., Shannon, P. M. & Readman, P. W. (2006). Crustal thinning, mantle exhumation and serpentinisation in the Porcupine Basin, offshore Ireland: evidence from wide-angle seismic data. Journal of the Geological Society, London, 163, 775-787, doi:10.1144/0016-76492005-079.

Pérez-Gussinyé, M. & Reston, T. J. (2001). Rheological evolution during extension at nonvolcanic rifted margins: onset of serpentinisation and development of detachments leading to continental breakup. Journal of Geophysical Research - Solid Earth, 106, 3961-3975, doi:10.1029/2000JB900325.

Pérez-Gussinyé, M., Morgan, J. P., Reston, T. J., & Ranero, C. R. (2006). The rift to drift transition at non-volcanic margins: Insights from numerical modelling. Earth and Planetary Science Letters, 244(1), 458-473.

Ranero, C. R., J. P. Morgan, K. McIntosh, and C. Reichert (2003), Bending-related faulting and mantle serpentinization at the Middle America trench, Nature, 425(6956), 367–373.

Readman, P. W., O'Reilly, B. M., Shannon, P. M. & Naylor, D. (2005). The deep structure of the Porcupine Basin, offshore Ireland, from gravity and magnetic studies. In Geological Society, London, Petroleum Geology Conference series, 6, 1047-1056, doi:10.1144/0061047.

Reid, I., & Jackson, H. R. (1981). Oceanic spreading rate and crustal thickness. Marine Geophysical Researches, 5(2), 165-172.

Reston, T. J., Pennell, J., Stubenrauch, A., Walker, I., & Perez-Gussinye, M. (2001). Detachment faulting, mantle serpentinisation, and serpentinite-mud volcanism beneath the Porcupine Basin, southwest of Ireland. Geology, 29(7), 587-590.

Reston, T. J., Gaw, V., Pennell, J., Klaeschen, D., Stubenrauch, A. & Walker, I. (2004). Extreme crustal thinning in the south Porcupine Basin and the nature of the Porcupine Median High: implications for the formation of non-volcanic rifted margins. Journal of the Geological Society, 161(5), 783-798, doi:10.1144/0016-764903-036.

Reston, T. J., Leythaeuser, T., Booth-Rea, G., Sawyer, D., Klaeschen, D., & Long, C. (2007). Movement along a low-angle normal fault: The S reflector west of Spain. Geochemistry, Geophysics, Geosystems, 8, n/a-n/a. http://doi.org/10.1029/2006GC001437

Sallarès, V., Gailler, A., Gutscher, M. A., Graindorge, D., Bartolomé, R., Gracia, E., Díaz, J., Dañobeitia, J.J. & Zitellini, N. (2011). Seismic evidence for the presence of Jurassic oceanic crust in the central Gulf

525 of Cadiz (SW Iberian margin). Earth and Planetary Science Letter, 311, 112-123,
526 doi:10.1016/j.epsl.2011.09.003.
527 Sandwell, D. T., R. D. Müller, W. H. F. Smith, E. Garcia, R. Francis, (2014) New global marine gravity model
528 from CryoSat-2 and Jason-1 reveals buried tectonic structure, Science, Vol. 346, no. 6205, pp. 65-67,
529 doi:10.1126/science.1258213
530 Stockwell, J. W. (1999), The CWP/SU: Seismic unix package, Comput.Geosci., 25(4), 415–419.
531 Tarantola, A., (1987). Inverse problem theory: methods for data fitting and model parameter estimation.
532 Elsevier Science, New York 613
533 Tate, M. P., White, N. & Conroy, J.-J. (1993). Lithospheric extension and magmatism in the Porcupine Basin
534 west of Ireland. Journal of Geophysical Research - Solid Earth, 98, 13905-13923,
535 doi:10.1029/93JB00890.
536 Tate, M. P. & Dobson, M. R. (1988). Syn-and post-rift igneous activity in the Porcupine Seabight Basin and
537 adjacent continental margin W of Ireland. Geological Society, London, Special Publications, 39, 309-
538 334, doi:10.1144/GSL.SP.1988.039.01.28.
539 Tutolo, B. M., Mildner, D. F., Gagnon, C. V., Saar, M. O., & Seyfried, W. E. (2016). Nanoscale constraints
540 on porosity generation and fluid flow during serpentinisation. Geology, 44(2), 103-106.
541 Watremez, L., Prada, M., Minshull, T., O'Reilly, B., Chen, C., Reston, T., Shannon, P., Wagner, G., Gaw, V.,
542 Klaeschen, D., Edwards, R., and Lebedev, S., (2016). Deep structure of the Porcupine Basin from
543 wide-angle seismic data. Geological Society, London, 8th Petroleum Geology Conference
544 Proceedings. doi:10.1144/PGC8.26
545 Weatherall P., K. M. Marks, M. Jakobsson, T. Schmitt, S. Tani, J. E. Arndt, M. Rovere, D. Chayes, V. Ferrini,
546 and R. Wigley (2015), A new digital bathymetric model of the world's oceans, Earth and Space
547 Science, 2, 331–345, doi: 10.1002/2015EA000107.
548 Wessel, P. & Smith, W. H. (1998). New, improved version of Generic Mapping Tools released. Eos,
549 Transactions American Geophysical Union, 79, 579-579, doi:10.1029/98EO00426
550 Whitmarsh, R. B., White, R. S., Horsefield, S. J., Sibuet, J. C., Recq, M., & Louvel, V. (1996). The ocean-
551 continent boundary off the western continental margin of Iberia: Crustal structure west of Galicia
552 Bank. Journal of Geophysical Research: Solid Earth, 101(B12), 28291-28314.

553 Zelt, C. A., & Forsyth, D. A. 1994. Modeling wide-angle seismic data for crustal structure: Southeastern
554 Grenville Province. Journal of Geophysical Research - Solid Earth, 99, 11687-11704,
555 doi:10.1029/93JB02764.

Figures

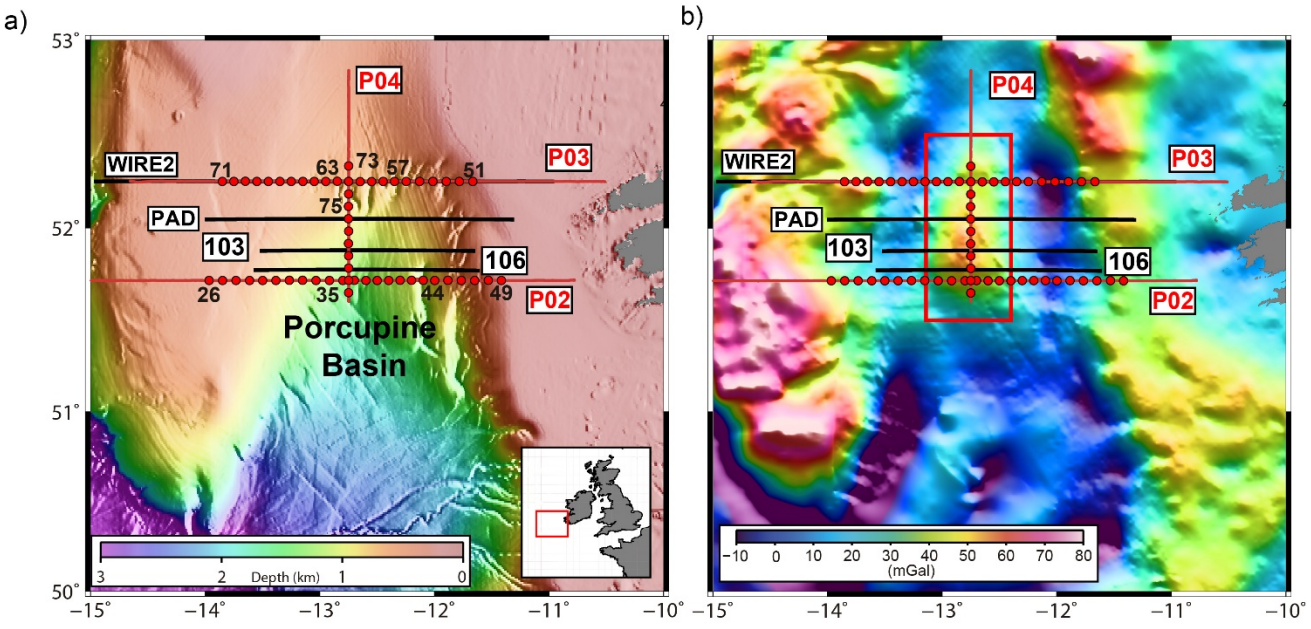

Figure 1.- (a) Bathymetry of the Porcupine Basin, southwest of Ireland (see inset), depicting the location of wide-angle seismic lines (red lines) and seismic reflection lines (black lines) used in this study. Wire2 was presented by *Klemper and Hobbs [1991]*. Seismic reflection lines 103 and 106 were previously presented by *Reston et al. [2001, 2004]*. Red circles are ocean-bottom receivers used to acquire wide-angle seismic data. Bathymetry data set is from *Weatherall et al. [2015]*. **(b)** Free air gravity anomaly map of the Porcupine Basin obtained from satellite data *[Sandwell et al., 2014]*. The red rectangle highlights the area of the gravity anomaly related to the Porcupine Arch.

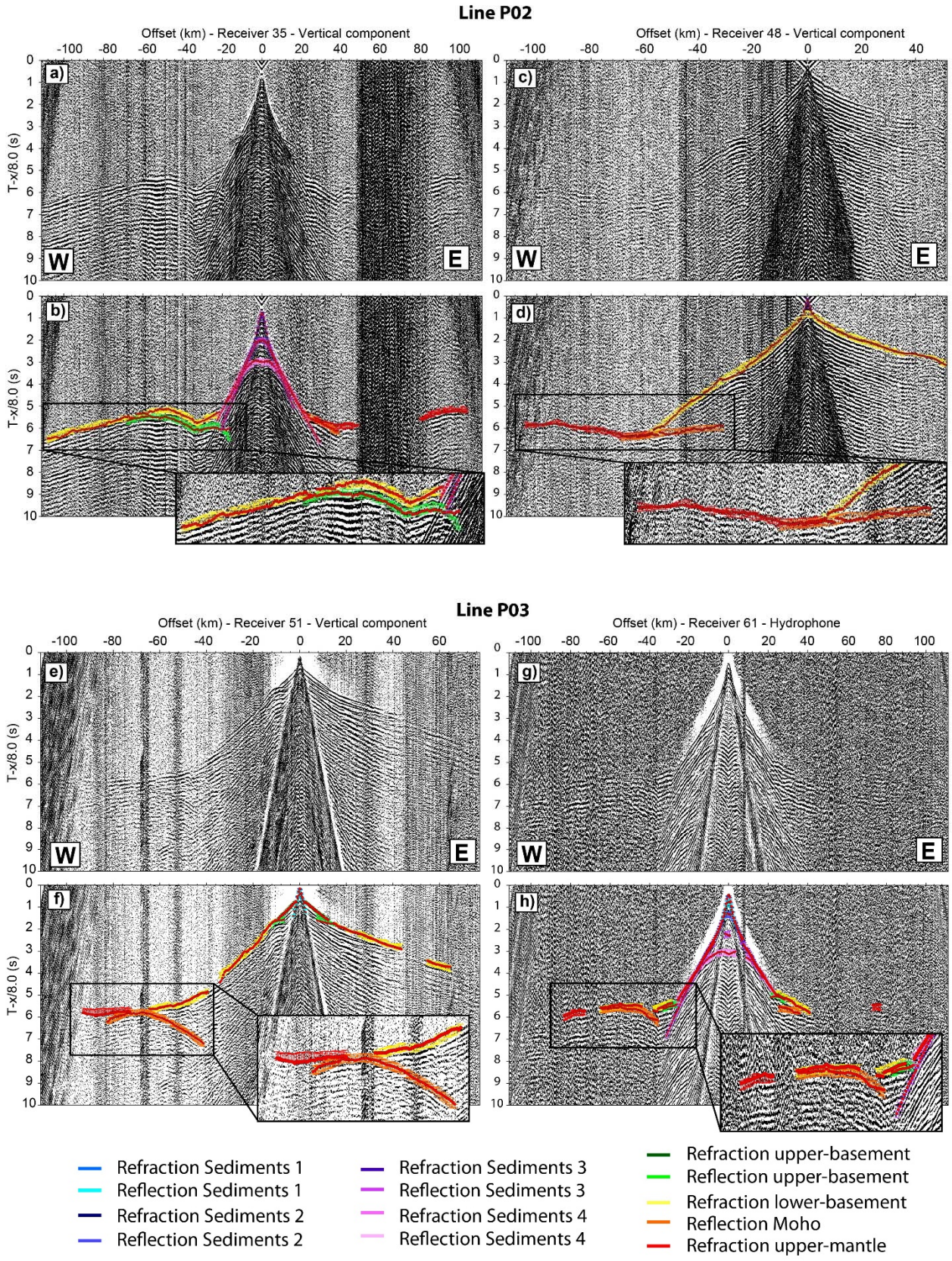

565

566 **Figure 2.-** Record sections of the vertical component of OBS 35 **(a, b)** and 48 **(c, d)** along P02, and
567 OBS 51 **(e, f)** and hydrophone 61 **(g, h)** along P03. Panels **b**, **d f**, and **h** show observed seismic phases
568 (coloured error bars), and calculated travel times (red dots). Record sections are reduced at 8 km/s.

569 Reflected sedimentary seismic phases were used to invert for those sedimentary interfaces shown in
570 Fig. A1.

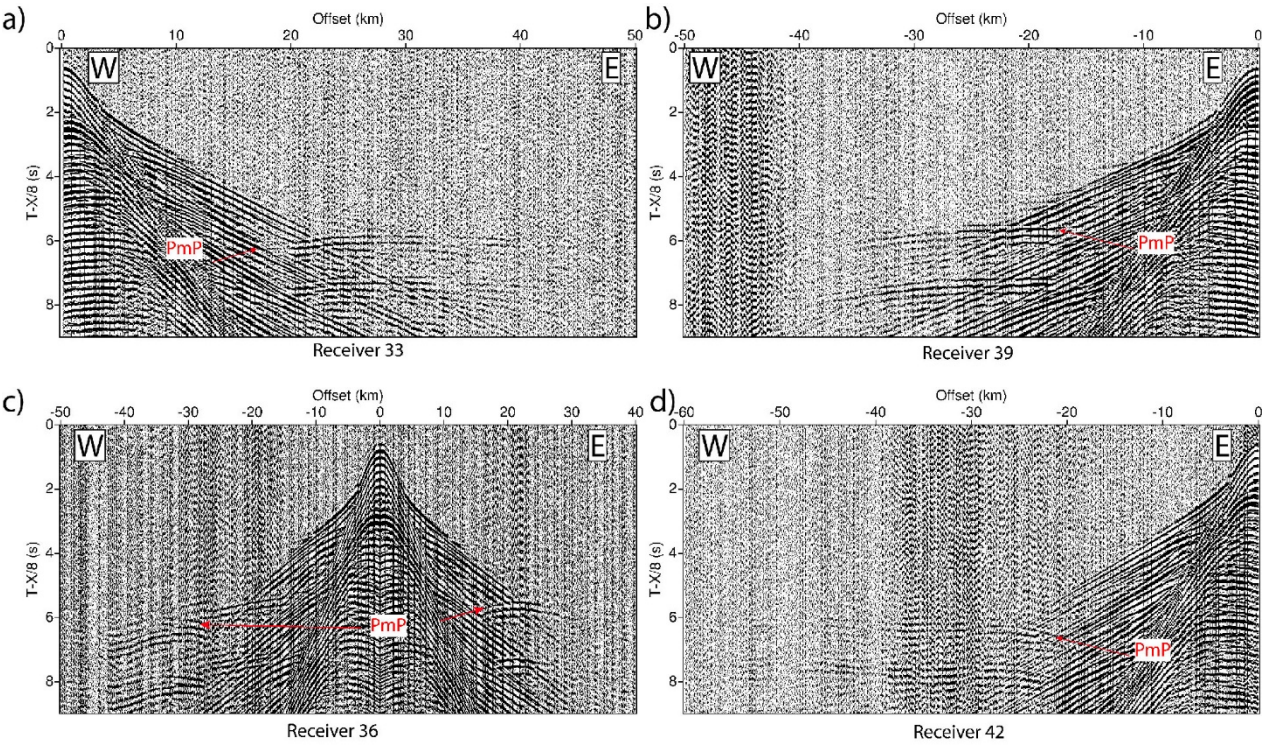

571

572 **Figure 3.-** Close up of record sections from hydrophone 33 **(a),** 39 **(b),** 36 **(c)** and 42 **(d)** along P02,
573 showing critical reflected phases interpreted as P_mP. Note that all record sections are reduced in time
574 using a velocity of 8 km/s.

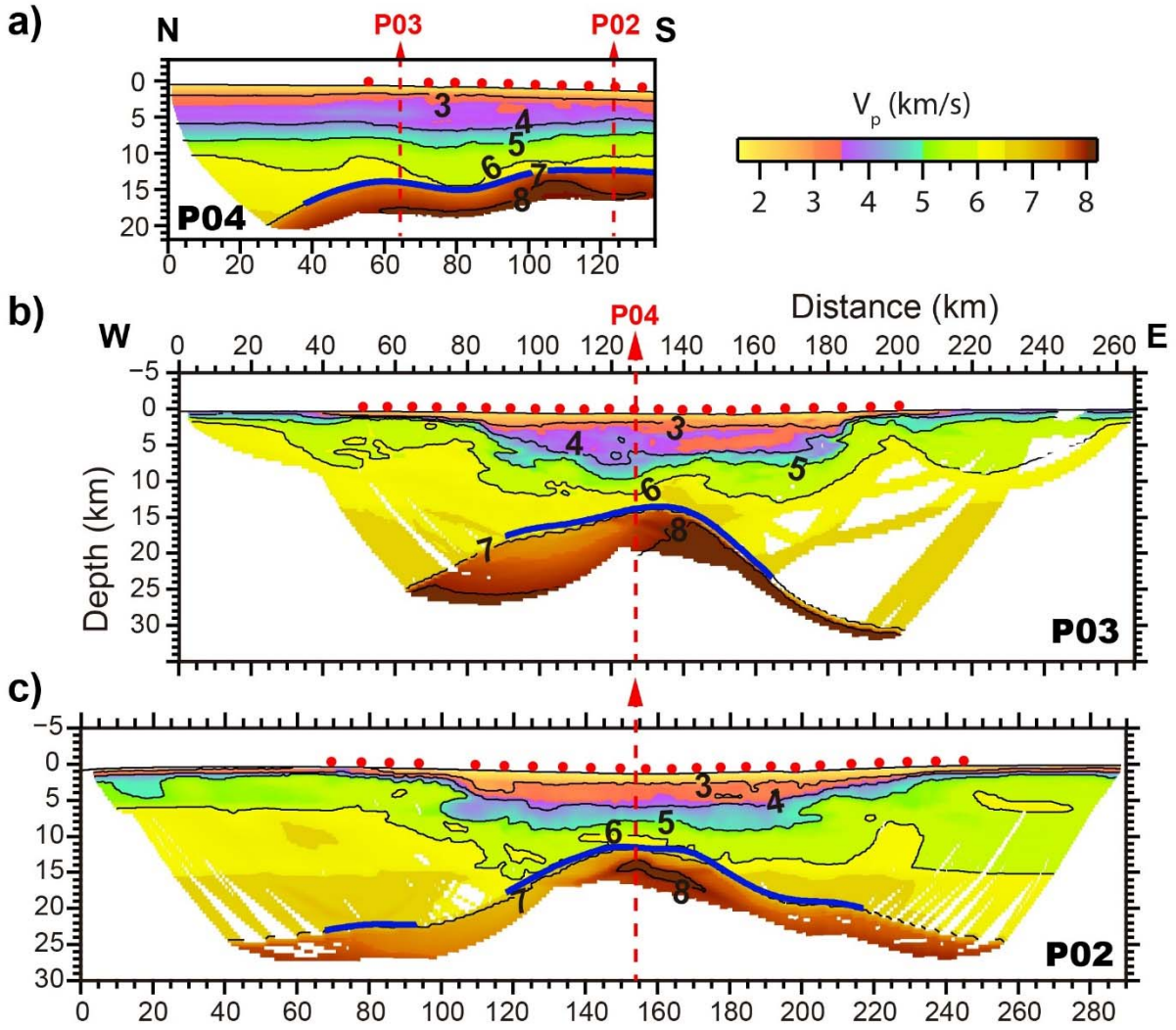

575

576 **Figure 4.- (a)** P-wave velocity (V_p) model P04 (strike line), **(b)** P03 and **(c)** P02 (dip lines). Seismic
577 velocities are shown where the derivative weight sum is > 0 (see Fig. A3 for more information on the
578 derivative weight sum). Note that the uppermost mantle is well covered by rays in the area of interest
579 for the study (i.e. the basin centre). Blue line is the P_mP-derived Moho (see Fig. A4 for ray tracing of
580 P_mP arrivals). Red dots are ocean-bottom seismometers/hydrophones.

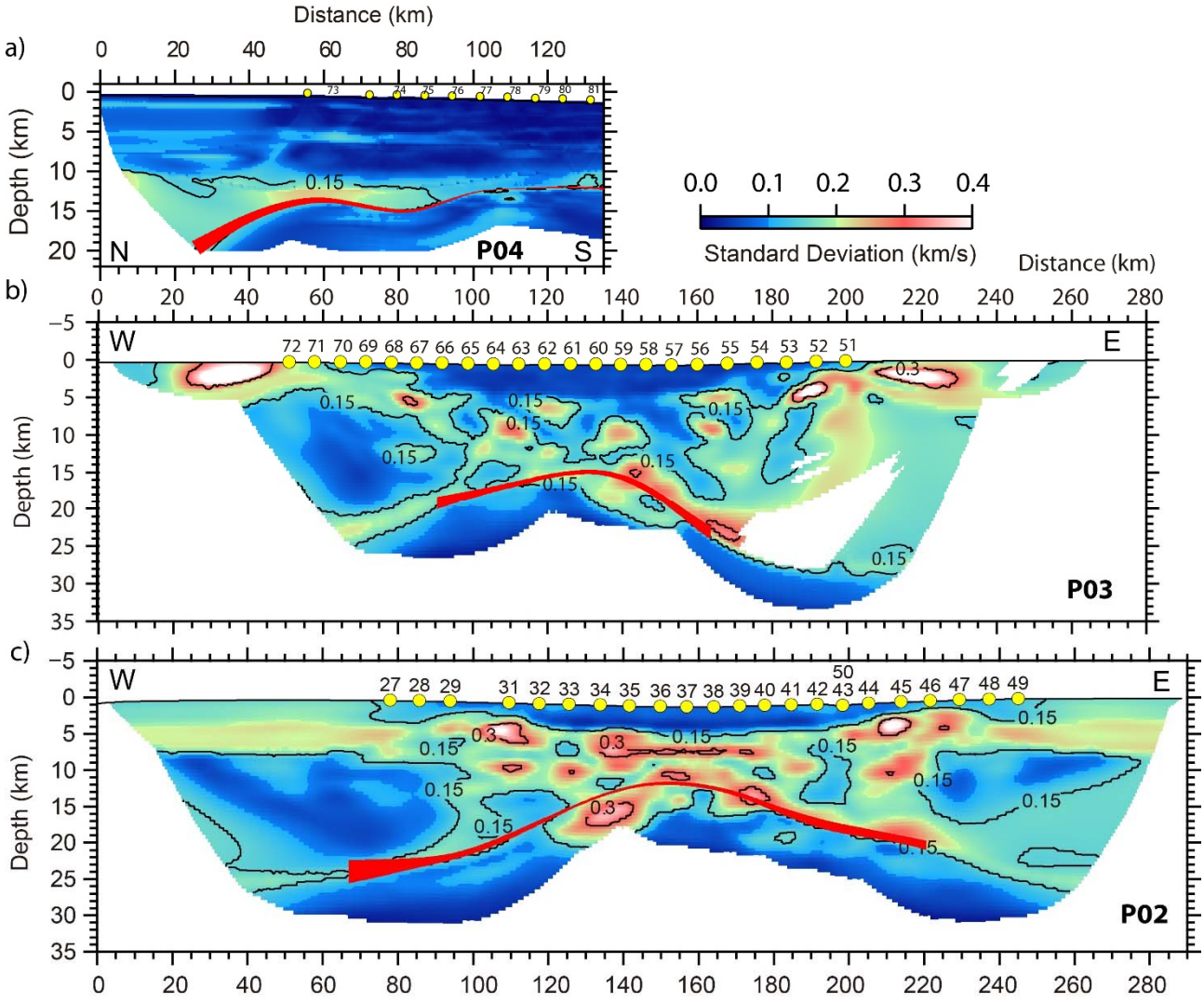

581

582 **Figure 5.-** Standard deviation of V_P values of the average solution of the Monte-Carlo analysis for
583 profiles P04 **(a)**, P03 **(b)**, and P02 **(c)**. The width of the red band shows the standard deviation of the
584 depth of the Moho.

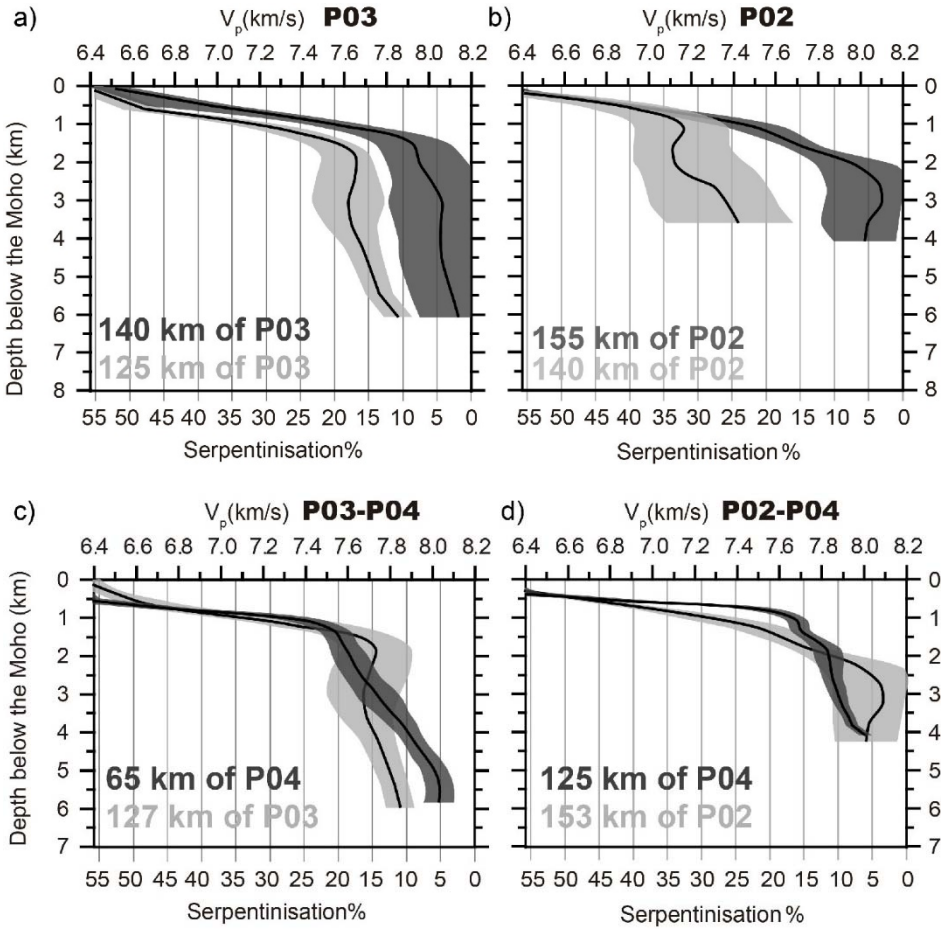

585

586 **Figure 6.-** 1D V_p vs depth diagrams of the uppermost mantle of models P03 **(a)** and P02 **(b)** showing
587 across-axis variations in mantle V_p. The degree of serpentinisation is derived from V_p using the
588 empirical relationship of *Carlson and Miller [2003]*, assuming a V_p of 8.2 km/s for unaltered
589 peridotite (i.e. 0% serpentinisation). The grey area represents the standard deviation computed from
590 the Monte-Carlo analysis, and the black solid lines are the vertical velocity structure extracted from
591 models in Fig. 4 at the profile distance given in the figure. We interpret the steep velocity gradient
592 (~1s^{-1}) in the first 2 km of each profile as a partially serpentinised, tectonically-controlled shear zone
593 between the crust and mantle, whereas the gentle gradient below (~0.1 s^{-1}) suggests a change to a less
594 pervasively deformed but still fractured zone with less serpentinisation. **(c)** and **(d)** are 1D V_p vs depth
595 diagrams comparing the seismic structure of profiles P03 and P02 with that of P04 at the intersection
596 point between models.

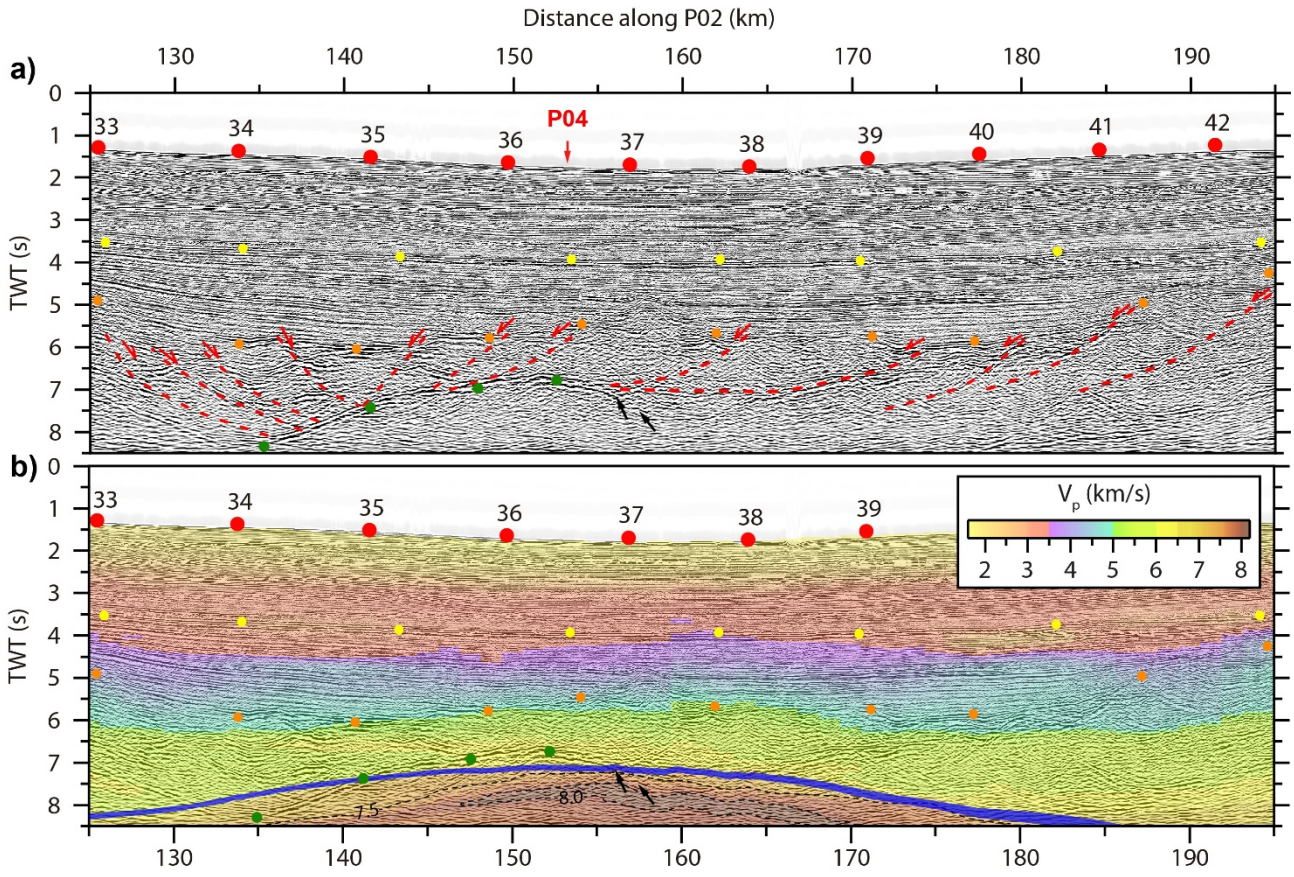

Figure 7.- (a) Time-migrated seismic reflection line 106 showing crustal faults modified from *Reston et al. [2004]*. Red dots are OBS/H, while yellow and orange dots depict the top of the Cretaceous unit and top of the syn-rift sequence, respectively. Green dots follow the P-detachment reflectivity there where it corresponds to the Moho. Black arrows show the eastward dipping reflectivity interpreted as the Moho by *Reston et al. [2001]*. Black arrows also depict the location where the P-detachment diverges from the Moho and becomes an intracrustal feature (see Fig. 2 in Reston et al., 2001). TWT: two-way time **(b)** Time-migrated seismic reflection line 106 overlaid by seismic velocities of model P02 converted from depth to two-way time assuming a near-vertical propagation. The width of the blue band shows the standard deviation of the depth of the WAS-derived Moho calculated in the Monte-Carlo analysis. See section 5.1 for detailed discussion on the mismatch between the WAS-derived Moho and the MCS-interpreted Moho observed along this image.

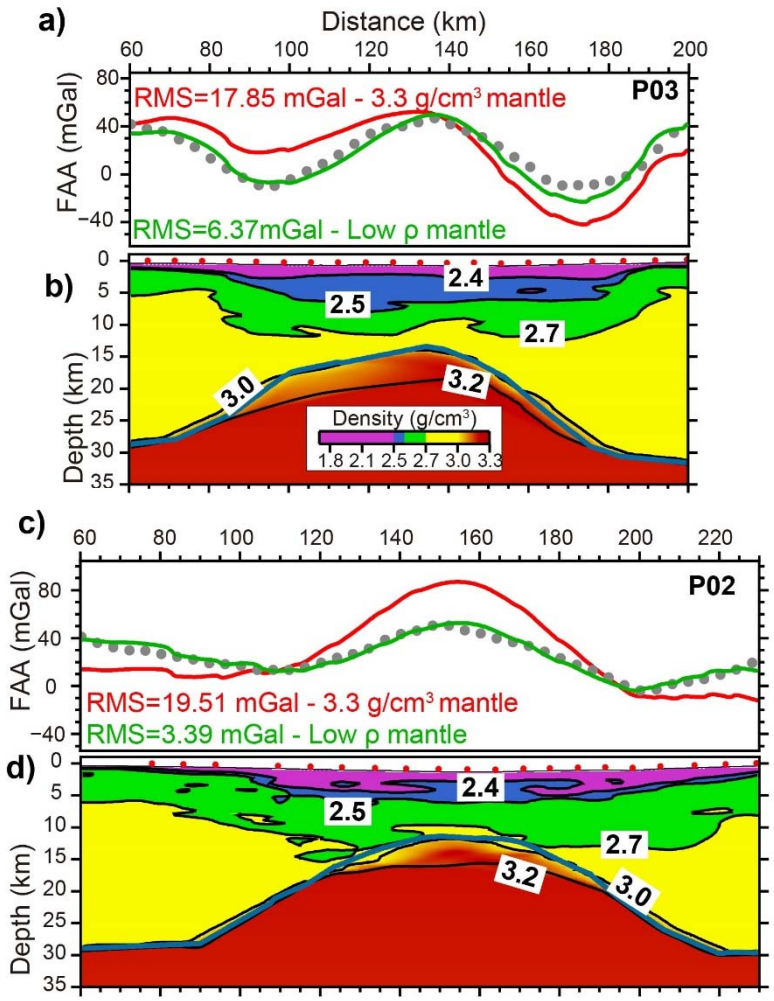

Figure 8.- (a) Observed free air gravity anomaly (FAA) from satellite measurements [*Sandwell et al., 2014]* (white circles) and synthetic anomaly (red & green lines) obtained along line P03. **(b)** Density model used to compute the best-fitted synthetic anomaly along P03 (green line). The Moho (blue line) has been extracted from velocity models in Fig. 4, and modified in the margins, where P_mP ray coverage was poor. The red line was obtained using the same density model as in (b) but with a 3.3 g/cm^3 homogeneous mantle density. **(c)** and **(d)** correspond to the same as (a) and (b), respectively, but along line P02. These results show that across-axis variations in mantle density are required to explain the gravity anomaly, and therefore support across-axis variations in the degree of serpentinisation.

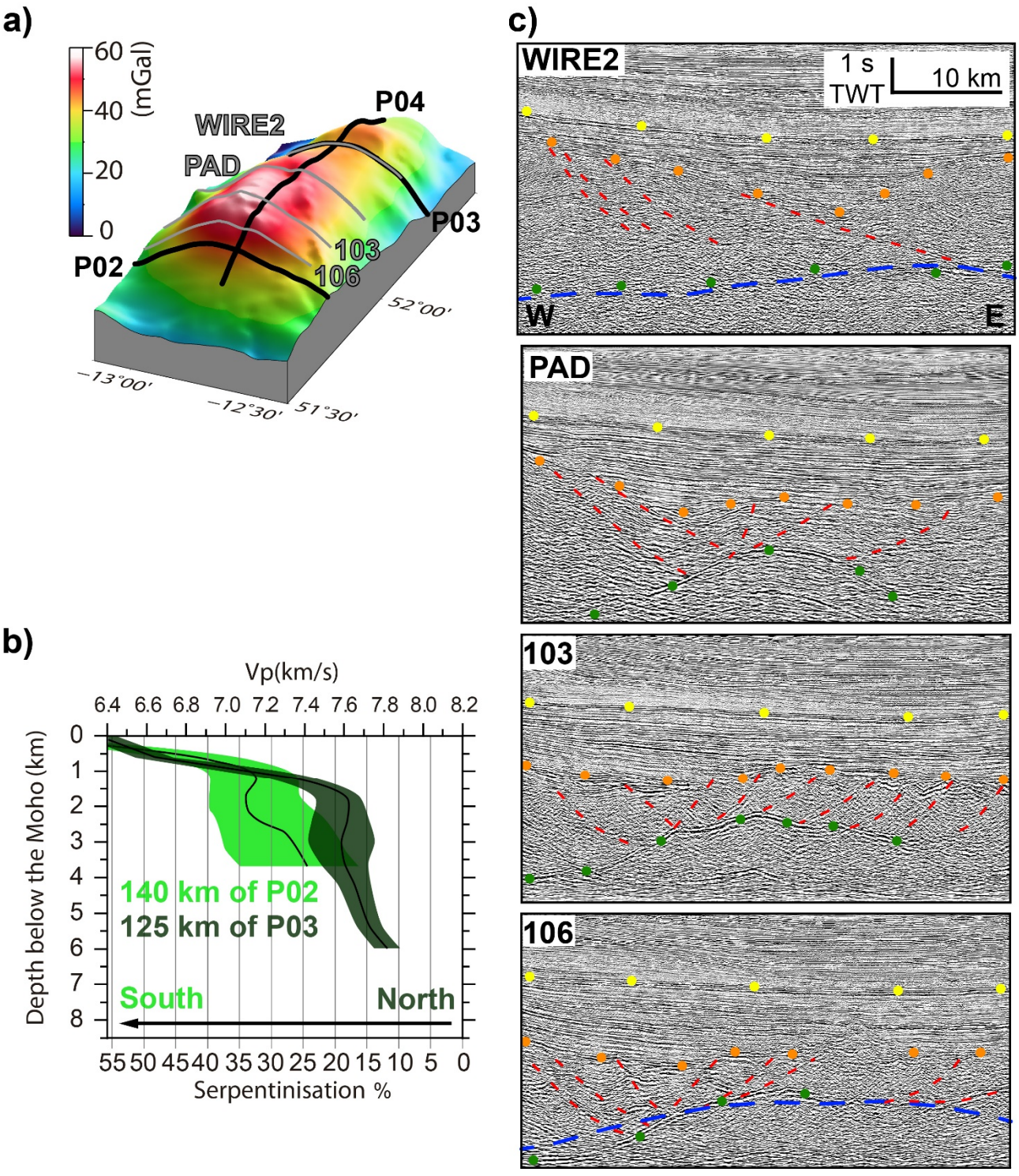

Figure 9.- (a) 3D view of the gravity anomaly highlighted in Fig. 1b. Thick black lines depict the location of WAS lines, whereas thin grey lines show the location of reflection lines used in this study. **(b)** 1D V_p vs depth diagrams of the upper mantle of models P02 and P03 showing how upper mantle V_p decreases southwards, suggesting an increasing degree of serpentinisation. The shaded areas show the standard deviations computed from the Monte-Carlo analysis. **(c)** From top (north) to bottom (south), time-migrated seismic reflection lines Wire2, PAD, 103 and 106, showing the increment of crustal faulting (dashed red lines) and variations of the P-detachment surface (green circles) along the

627 basin axis. Blue dashed line is the Moho derived from WAS data. Orange dots depict top of syn-rift,
628 while yellow dots show top Cretaceous. Wire2 was previously discussed by *Klemper and Hobbs*
629 *[1991]* and *Watremez et al. [2016]*.

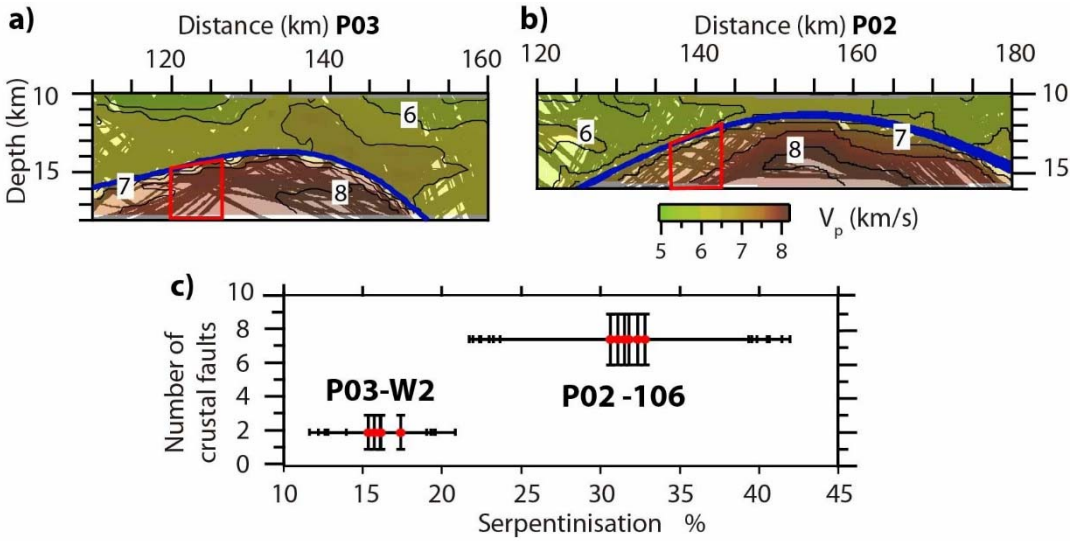

630

631 **Figure 10.- (a, b)** Ray coverage of the lower crust and uppermost mantle along lines P03 and P02,
632 respectively. The width of the blue band shows the standard deviation of the depth of the Moho, while
633 the red box depicts the region chosen to derive the vertically averaged degree of serpentinisation
634 shown in (d). These areas are selected because they are constrained by comparatively high ray
635 coverage, and because they are located beneath crustal faulting potentially responsible for mantle
636 hydration. **(c)** Vertically averaged V_p-derived degree of serpentinisation from the red box in (b) and
637 (c) vs the number of crustal faults interpreted from seismic reflection lines Wire2 (coincident to P03)
638 and 106 (neighbour to P02). The degree of serpentinisation was derived from V_p using the empirical
639 relationship of *Carlson and Miller [2003]*. The interpreted amount of faulting is displayed within a
640 range of uncertainty based on observations from seismic lines in Fig. 9c. The uncertainty of the degree
641 of serpentinisation is derived from results of the Monte-Carlo analysis in Fig. 5.

642

643 Figures A1 to A4 provide information about the layer stripping sequence followed to obtain the
644 tomographic models P04, P02, and P03, as well as ray tracing information of each model. Tables A1
645 to A3 contain information regarding modelling statistics of each tomographic model.

646

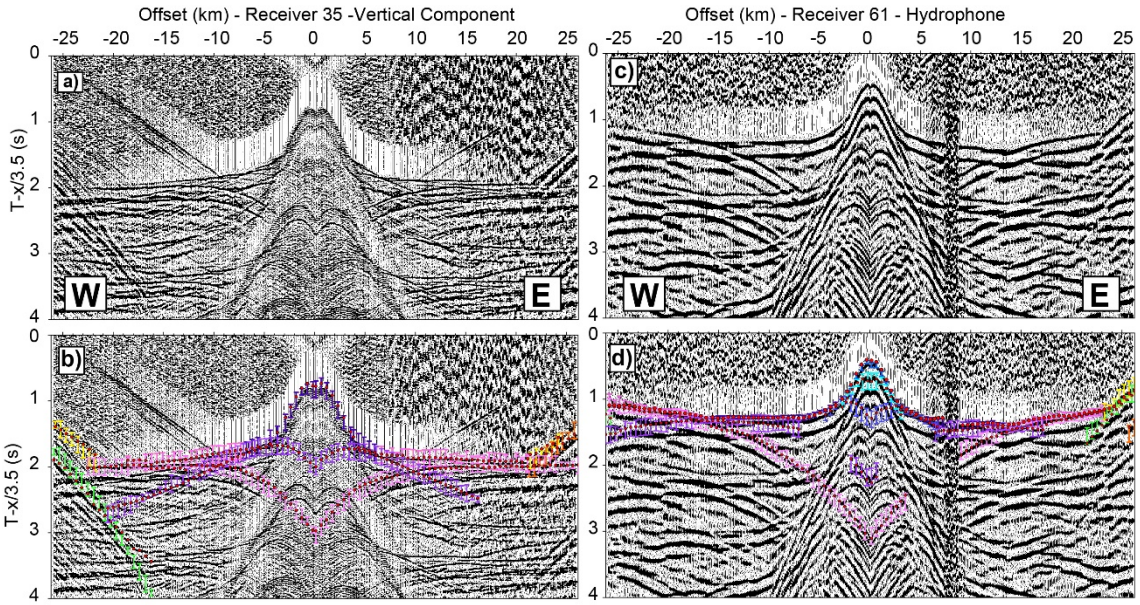

647

648 **Figure A1.-** Close up of record sections of the vertical component of OBS 35 **(a, b)** along P02, and
649 hydrophone 61 **(c, d)** along P03. Panels **b**, **d** show observed seismic phases (coloured error bars, see
650 Fig. 2 for colour code), and calculated travel times (red dots). Record sections are reduced at 3.5 km/s.
651 Reflected sedimentary seismic phases were used to invert for those sedimentary interfaces shown in
652 Fig. A2.

a)

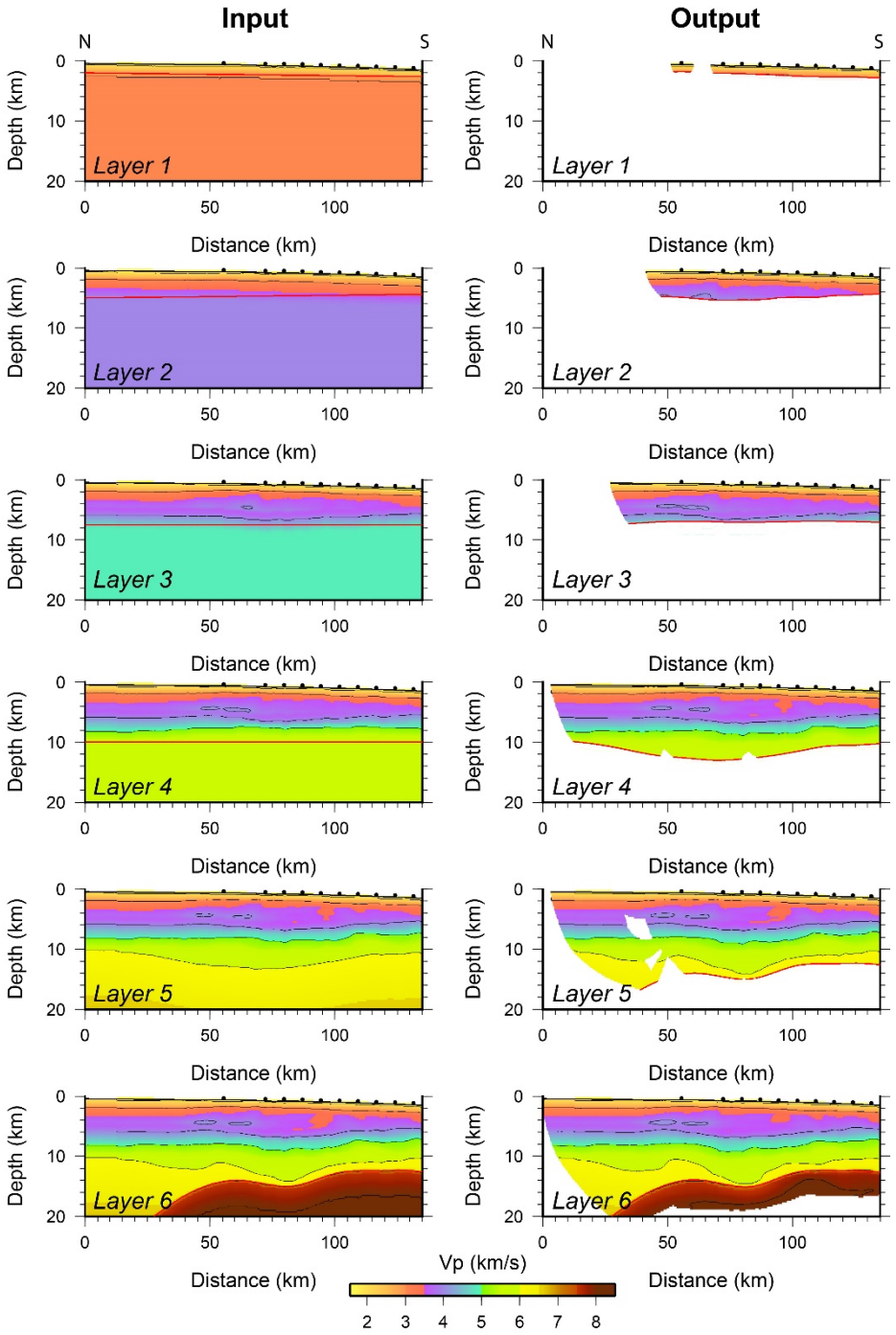
Input
Output
N
S
Depth (km)
Distance (km)
Layer 1
Layer 2
Layer 3
Layer 4
Layer 5
Layer 6
Vp (km/s)
2 3 4 5 6 7 8

653

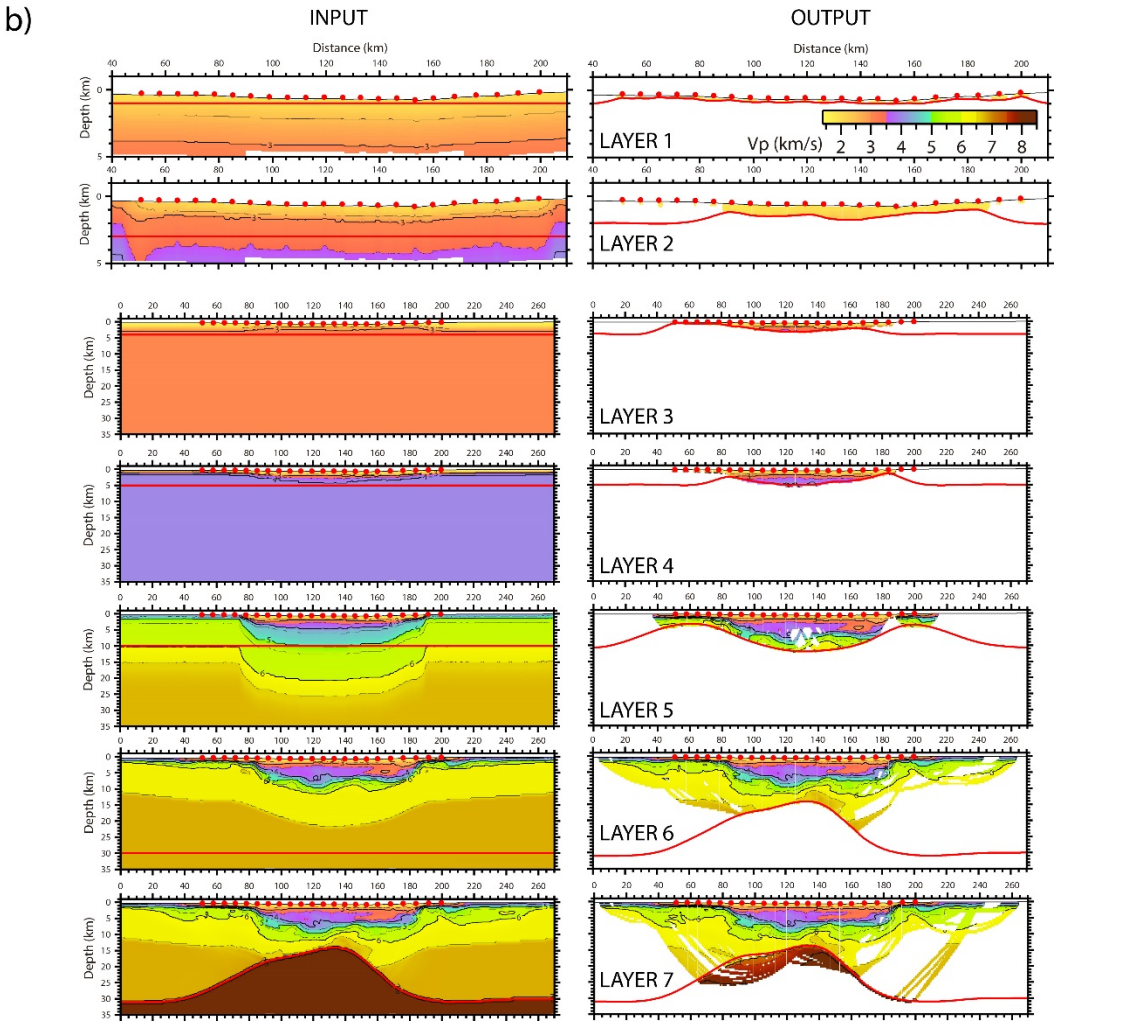

654

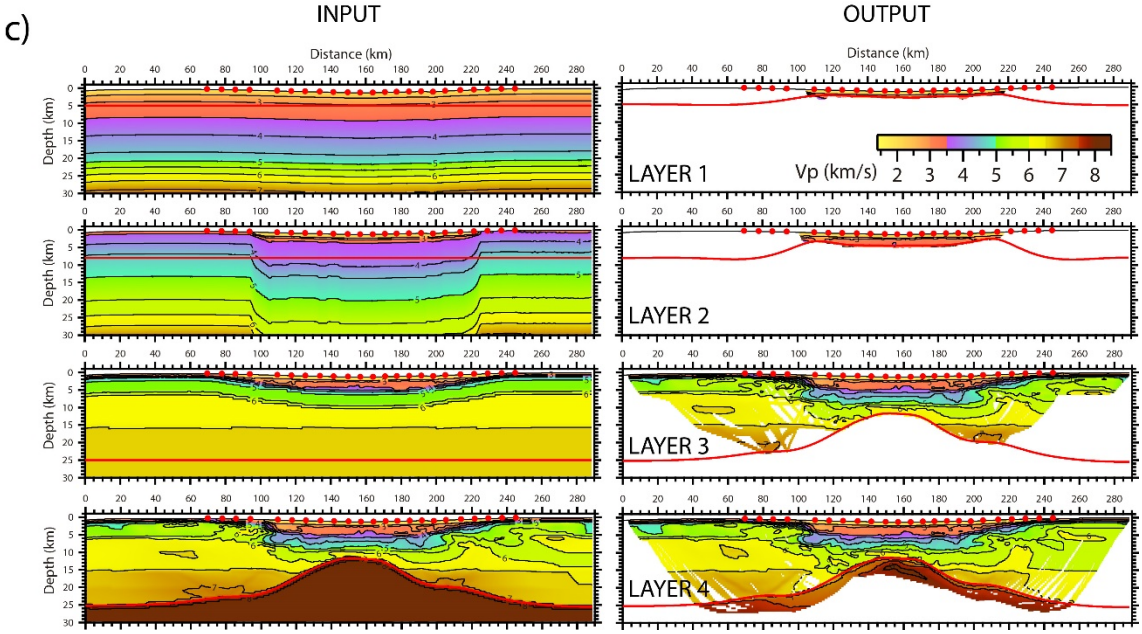

655

656 **Figure A2.-** Layer stripping sequence of models P04 **(a)**, P03 **(b)** and P02 **(c)**. This sequence
657 illustrates the construction of each model. Examples of travel times used to invert for sedimentary
658 interfaces are shown in Fig. 2.

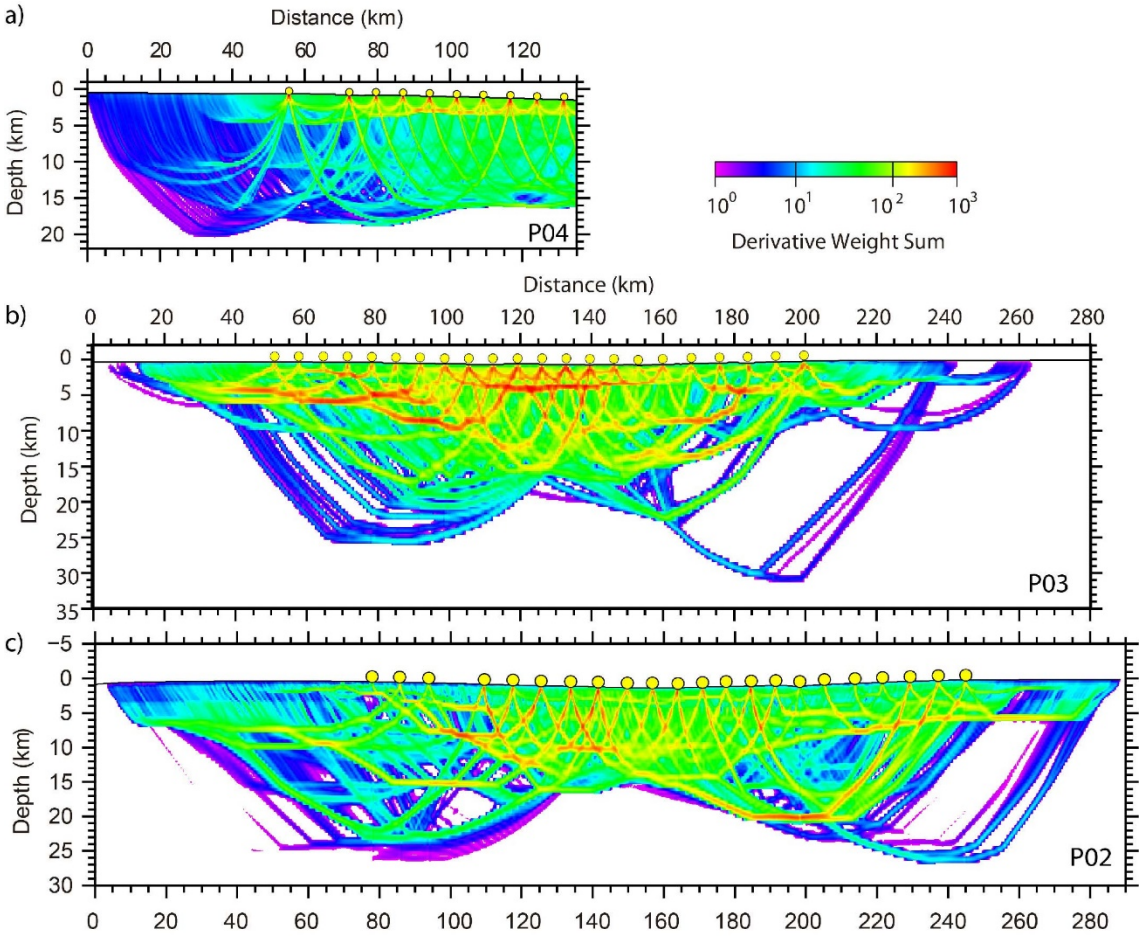

659

660

661 **Figure A3.-** Derivative weight sum of profiles P04 **(a)**, P03 **(b)** and P02 **(c)**. These images provide a
662 quantitative estimate of the ray density along this line

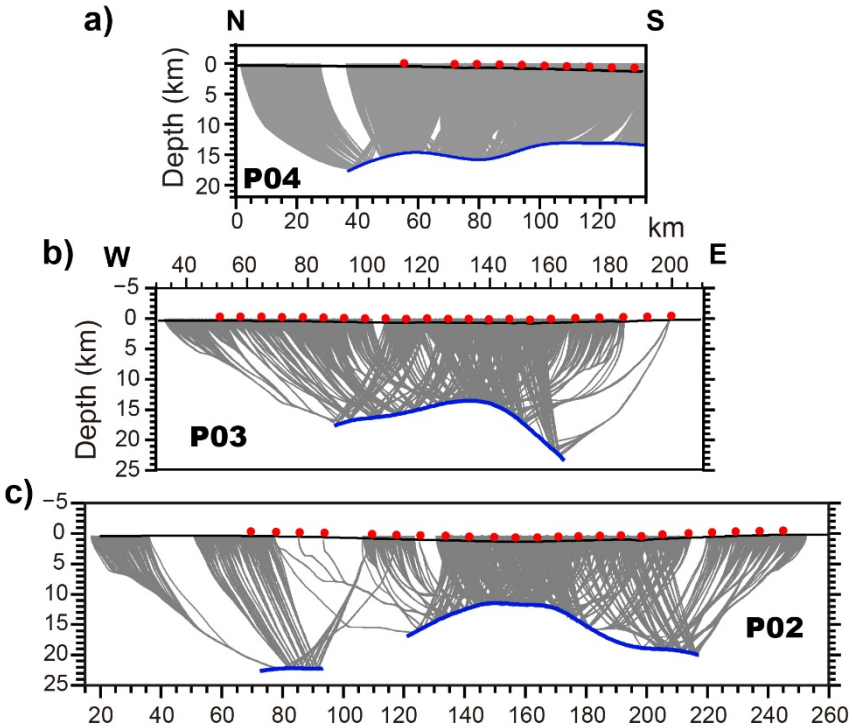

663

664 **Figure A4.-** Ray tracing of P_mP arrival times of WAS profiles P04 **(a)**, P03 **(b)** and P02 **(c).** Blue
665 thick line shows the inverted geometry of the Moho, whereas red dots are ocean-bottom receivers.
666 Black line depicts the seafloor topography.

667

Table A1. *Modelling statistics for P02. The "refr" (refractions), "refl" (reflections)" and "all" subscripts refer to the parts of dataset considered.*

Step	Iteration*	N_{refr}†	N_{refl}†	$t_{RMS\text{-}refr}$‡	$t_{RMS\text{-}refl}$‡	$t_{RMS\text{-}all}$‡	χ^2_{refr}§	χ^2_{refl}§	χ^2_{all}§
1	12	1,658	2,404	85	48	68	1.09	0.60	0.80
2	14	3,990	4,782	55	66	61	0.35	0. 90	0.67
3	14	14,475	3,316	76	60	73	0.79	0.94	0.82
4	14	18,493	3,316	75	69	74	1.00	1.06	1.01

668 *Iteration chosen to build the input model of next step (or final model for step 6).
669 †Numbers of picks used for the modelling.
670 ‡Root mean squared travel-time residuals, in milliseconds.
671 §Normalised chi-squared.

672

Table A2. *Modelling statistics for P03. The "refr" (refractions), "refl" (reflections)" and "all" subscripts refer to the parts of dataset considered.*

Step	Iteration*	N_{refr}†	N_{refl}†	$t_{RMS\text{-}refr}$‡	$t_{RMS\text{-}refl}$‡	$t_{RMS\text{-}all}$‡	χ^2_{refr}§	χ^2_{refl}§	χ^2_{all}§
1	4	654	1,050	32	31	32	1.18	0.22	0.58
2	9	978	886	25	32	28	0.82	0.13	0.49
3	9	2,399	3,445	20	38	32	0.48	0.25	0.35
4	9	4,410	4,124	17	29	23	0.29	0.12	0.21
5	9	5,955	1,819	36	83	51	0.98	1.04	0.99
6	4	15,580	3,004	58	95	65	0.60	1.11	0.69
7	4	17,348	3,004	61	84	65	0.62	0.91	0.66

673 *Iteration chosen to build the input model of next step (or final model for step 6).
674 †Numbers of picks used for the modelling.
675 ‡Root mean squared travel-time residuals, in milliseconds.
676 §Normalised chi-squared.

677

Table A3. *Modelling statistics for P04. The "refr" (refractions), "refl" (reflections)" and "all" subscripts refer to the parts of dataset considered.*

Step	Iteration*	N_{refr}†	N_{refl}†	$t_{RMS\text{-}refr}$‡	$t_{RMS\text{-}refl}$‡	$t_{RMS\text{-}all}$‡	χ^2_{refr}§	χ^2_{refl}§	χ^2_{all}§
1	2	1,515	1,507	11	22	17	0.28	0.28	0.28
2	2	4,634	5,159	14	30	24	0.19	0.41	0.30
3	2	5,252	2,676	20	52	34	0.19	0.83	0.41
4	2	8,979	4,658	38	67	50	0.29	0.81	0.47
5	2	8,979	5,241	33	50	40	0.23	0.39	0.29
6	1	16,467	5,241	63	49	60	0.45	0.39	0.44

678 *Iteration chosen to build the input model of next step (or final model for step 6).
679 †Numbers of picks used for the modelling.
680 ‡Root mean squared travel-time residuals, in milliseconds.
681 §Normalised chi-squared.

682

683

684